



**HAL**  
open science

## Global Statistics of Ice Microphysical and Optical Properties at Tops of Optically Thick Ice Clouds

Bastiaan van Dierenhoven, Andrew S. Ackerman, Ann M. Fridlind, Brian Cairns, Jérôme Riedi

► **To cite this version:**

Bastiaan van Dierenhoven, Andrew S. Ackerman, Ann M. Fridlind, Brian Cairns, Jérôme Riedi. Global Statistics of Ice Microphysical and Optical Properties at Tops of Optically Thick Ice Clouds. Journal of Geophysical Research: Atmospheres, 2020, 125, 10.1029/2019JD031811 . insu-03686302

**HAL Id: insu-03686302**

**<https://insu.hal.science/insu-03686302>**

Submitted on 3 Jun 2022

**HAL** is a multi-disciplinary open access archive for the deposit and dissemination of scientific research documents, whether they are published or not. The documents may come from teaching and research institutions in France or abroad, or from public or private research centers.

L'archive ouverte pluridisciplinaire **HAL**, est destinée au dépôt et à la diffusion de documents scientifiques de niveau recherche, publiés ou non, émanant des établissements d'enseignement et de recherche français ou étrangers, des laboratoires publics ou privés.

Copyright

# JGR Atmospheres

## RESEARCH ARTICLE

10.1029/2019JD031811

### Key Points:

- We present a global assessment of collocated cloud top ice size, shape, and scattering property observations
- Ice scattering asymmetry parameters are found to decrease with increasing effective radius, contrary to commonly used optical models
- The observations suggest that the temperature dependence of cloud top ice size and shapes are commonly dominated by vapor growth processes

### Supporting Information:

- Supporting Information S1

### Correspondence to:

B. van Dierenhoven,  
bv2154@columbia.edu

### Citation:

van Dierenhoven, B., Ackerman, A. S., Fridlind, A. M., Cairns, B., & Riedi, J. (2020). Global statistics of ice microphysical and optical properties at tops of optically thick ice clouds. *Journal of Geophysical Research: Atmospheres*, 125, e2019JD031811. <https://doi.org/10.1029/2019JD031811>

Received 9 OCT 2019

Accepted 28 FEB 2020

Accepted article online 03 MAR 2020

©2020. American Geophysical Union.  
All Rights Reserved.

## Global Statistics of Ice Microphysical and Optical Properties at Tops of Optically Thick Ice Clouds

Bastiaan van Dierenhoven<sup>1,2</sup> , Andrew S. Ackerman<sup>2</sup> , Ann M. Fridlind<sup>2</sup> , Brian Cairns<sup>2</sup> , and Jérôme Riedi<sup>3</sup> 

<sup>1</sup>Center for Climate System Research, Columbia University, New York, NY, USA, <sup>2</sup>NASA Goddard Institute for Space Studies, New York, NY, USA, <sup>3</sup>Univ. Lille, CNRS, UMR 8518 - LOA - Laboratoire d'Optique Atmosphérique, Lille, France

**Abstract** The sizes and shapes of ice crystals in clouds affect fundamental microphysical processes, such as sedimentation and aggregation, as well as their optical properties. The evolution of ice crystal size and shape depends on temperature and supersaturation, as well as on other processes that may lead to various coexisting complex shapes. Here we present a global assessment of collocated size and shape characteristics and shortwave scattering properties of ice crystals at the tops of optically thick clouds inferred from space-borne multiwavelength reflectance measurements and multiangle polarimetry. The results indicate systematic covariations of ice size, shape, and distortion, as well as variations with temperature that can be plausibly related to simplified ice crystal growth theory and in situ and laboratory data. This simplicity may be attributable to the temperature dependence of cloud top ice size and shapes commonly being dominated by vapor growth at conditions similar to those at cloud top. Such a conclusion may be viewed as somewhat surprising given the expectation that ice properties at cloud top will be an integral manifestation of processes occurring at lower levels within updrafts. We also find that, contrary to commonly used models, ice scattering asymmetry parameters decrease with increasing effective radius, reducing sensitivity of cloud reflectance to particle size.

**Plain Language Summary** The sizes and shapes of ice crystals in cold clouds influence how these clouds evolve and how much sunlight they reflect. It is relatively well understood how temperature and humidity affect the sizes and shapes of ice crystals as they grow directly from water vapor. However, our understanding of the influence of other complex processes on ice crystal shape and size in natural clouds is less developed. Using combined measurements of two satellites, we investigate the variation of sizes and shapes in the tops of thick ice clouds on a global scale. We find that how observed ice crystal size and shape varies with temperature can be well explained by the theory on ice crystals growing from water vapor. This simplicity is somewhat surprising and may indicate that the many more complex ice growth processes have limited effect on the variation of ice shape and size at the tops of clouds. The analysis also suggests that some common assumptions on the influence of ice crystal size and shape on the amount of sunlight that is reflected by ice clouds need to be revisited. Our results can serve as a reference for improving the representation of ice clouds in climate models.

## 1. Introduction

The dominating contribution from uncertainties in cloud feedbacks and aerosol-cloud interactions to overall uncertainty in climate model projections is long-standing (Boucher et al., 2013). Although perhaps more attention has been directed toward liquid-phase clouds, some recent efforts have emphasized the complex physics of glaciated and mixed-phase clouds and the need to improve their representation in climate models (Storelvmo, 2017; Waliser et al., 2009). The sizes and shapes of ice crystals affect fundamental microphysical processes, such as sedimentation, vapor growth, and aggregation, as well as cloud optical properties. The evolution of shapes and ice growth rates are known to depend on temperature and supersaturation. Laboratory measurements show that vapor growth rates at a given water saturation generally increase with increasing supersaturation and decrease with departures of temperature from about 255 K (Bailey & Hallett, 2004; Fukuta & Takahashi, 1999). However, many additional processes increase the variability of ice crystal populations (Bailey & Hallett, 2009). Furthermore, the shapes and sizes of ice crystals may depend on nucleation specifics, ice multiplication processes, and the properties of ice nucleating particles (Bailey & Hallett, 2004; Schnaiter et al., 2016). Although the fundamental shape of water ice crystals is the hexagonal

prism, the variability of their aspect ratios and of polycrystalline, aggregated, and sublimated shapes in natural ice clouds is virtually limitless, and many shapes can coexist in the same cloud volume (Bailey & Hallett, 2009; Lawson et al., 2019). Furthermore, microscale roughness structures on crystal surfaces and other crystal distortions appear ubiquitous and substantially affect crystal scattering properties (Butterfield et al., 2017; van Diedenhoven, Ackerman, et al., 2014; Fu, 2007; Magee et al., 2014; Neshyba et al., 2013; Pfalzgraff et al., 2010). Recent studies suggest that levels of roughness and complexity increase with ice crystal growth rate but may also depend on humidity, temperature, and nucleation mechanism (Bacon et al., 2003; Schmitt et al., 2016; Schnaiter et al., 2016; Voigtländer et al., 2018).

The solar reflectance, transmittance, and absorptance of a cloud layer with a given ice water path are primarily determined by the effective radius ( $r_e$ ) and scattering asymmetry parameter ( $g$ ) of the ice crystals (Platt, 1997; Stephens et al., 2001). In turn,  $g$  at visible wavelengths is primarily determined by crystal shape and additionally by  $r_e$  in the shortwave infrared (van Diedenhoven, Ackerman, et al., 2014). Since general circulation models generally predict ice water paths, it is crucial to obtain robust constraints on  $r_e$  and  $g$  to derive ice cloud radiative properties. Previous estimates show that uncertainties of optical thickness and asymmetry parameter need to be generally less than about 10% and 5%, respectively, to determine the top of atmosphere fluxes in atmospheres overcast by ice cloud to within 5%, but these uncertainty limits depend on many factors (Vogelmann & Ackerman, 1995). Since optical thickness is generally linearly computed from given ice water path and  $r_e$ , this also implies that the required uncertainty on  $r_e$  is on the order of 10%. Shortwave reflectance measurements provide a robust means of inferring  $r_e$  at cloud tops (Platnick et al., 2017) but rely on assumptions of ice scattering properties, most importantly assumed  $g$  (Holz et al., 2016). In situ and satellite measurements have suggested that rough or distorted compact crystals with smooth phase functions and visible asymmetry parameters near 0.75 dominate globally (Holz et al., 2016; Järvinen et al., 2018) (see van Diedenhoven, 2018, for an overview on ice shape remote sensing). However, the presented interquartile and full ranges of such measurements are large, indicating substantial variation of crystal shape, distortion, and scattering properties regionally and globally. Ignoring such variability in radiative transfer calculations may lead to biases that depend on location, cloud type, and other factors.

Here we provide, to our knowledge, a first global assessment of collocated effective radii, shape characteristics, and scattering properties of ice crystals near the tops of optically thick clouds inferred from satellite measurements. These retrievals are based on the general conclusion from past calculations that simple hexagonal prisms can be used as radiative proxies for complex ice crystals (van Diedenhoven, Ackerman, et al., 2014; Fu, 2007; Iaquina et al., 1995; Um & McFarquhar, 2007, 2009). In addition to effective radius, the aspect ratio of hexagonal components of crystals and a crystal distortion parameter are retrieved, from which the asymmetry parameter is in turn derived. We analyze 1 year of combined multiangle polarization and shortwave infrared measurements of the Polarization and Directionality of the Earth's Reflectances (POLDER) and Moderate Resolution Imaging Spectroradiometer (MODIS) instruments at a spatial resolution of about  $6 \times 6 \text{ km}^2$ . Since these combined measurements are extremely sensitive to spherical water drops within approximately the top optical depth anywhere in an observational footprint, a robust filtering of liquid-phase cloud tops can be made allowing ice properties for cloud top temperatures up to nearly 273 K to be included in this study (van Diedenhoven, Fridlind, et al., 2012; Riedi et al., 2010). We analyze the covariation of these ice cloud properties and their variation as a function of cloud top temperature. We relate our findings to ice crystal growth theory and laboratory and in situ measurements. Furthermore, we quantify variations in associated cloud radiative properties.

Methods and data are described in section 2. Section 3 presents the results, separated by discussions on the global statistics and vertical variation of ice properties (3.1), covariation of ice properties (3.2), their variation with cloud optical thickness (3.3), and the scaled mass extinction coefficients that determine cloud visible reflectivity for a given ice water path (3.4). Conclusions are given and discussed in section 4.

## 2. Methods and Data

Ice crystal component aspect ratio, distortion parameter, and asymmetry parameter are retrieved from multiangle polarized reflectances at 865 nm measured by POLDER satellite instrument on the Polarization and Anisotropy of Reflectances for Atmospheric Sciences coupled with Observations from a Lidar (PARASOL)

platform. The method and its application to POLDER are described in detail in previous publications (van Diedenhoven, Cairns, et al., 2012; van Diedenhoven, Fridlind, et al., 2014). Simple hexagonal ice prisms are used as proxies for natural distributions of more complex ice crystals. The aspect ratio and distortion parameters of the proxy hexagonal ice prisms are inferred by determining the lowest relative root-mean-squared difference (RRMSD, as defined by van Diedenhoven, Cairns, et al., 2012; see also Appendix A) between measurements and simulated values within a look-up table (LUT) of simulated multi-directional polarized reflectances. The LUT is calculated by assuming individual hexagonal particles with varying aspect ratios (51 values in total varying between 0.02 and 1 for both columns and plates) and distortion parameters (15 values in total varying between 0 and 0.7). Aspect ratio of the proxy hexagonal ice prisms is defined as the prism length divided by prism width for plates and the inverse of that for columns, leading to aspect ratio values equal or below unity (van Diedenhoven, Ackerman, et al., 2016). The distortion parameter is defined by the parameterization of Macke et al. (1996) and is approximately equivalent to other commonly used distortion parameters (Geogdzhayev & van Diedenhoven, 2016; Neshyba et al., 2013). The distortion parameter is a proxy for randomization of the crystal shape caused by a number of factors such as large-scale crystal distortion and complexity, microscale surface roughness, and impurities within the crystals (Hong & Minnis, 2015; Liu et al., 2014; Neshyba et al., 2013). For every included POLDER footprint, the combination of aspect ratio and distortion value that leads to the best fit with the measurements is considered the retrieved set, and, in turn, the asymmetry parameter corresponding to this set is the inferred value. The method has been evaluated with simulated (van Diedenhoven, Cairns, et al., 2012; van Diedenhoven, Ackerman, et al., 2016) and airborne measurements (van Diedenhoven et al., 2013). In general, the method is shown to be able to retrieve the average asymmetry parameter of a collection of ice crystals to within 5% per observation, largely independent of calibration errors, sampling density of scattering angles, and random noise in the measurements. A study using simulations based on bullet rosettes with varying aspect ratios and distortion levels revealed that the average component aspect ratios were generally retrieved within 20–40% and distortion parameters within 0.05. We previously demonstrated that retrieved aspect ratios and distortion parameters are consistent with ensemble averaged values (if aspect ratios are defined with values equal or below unity for both plates and columns) and distributions dominated by smooth or rough surfaces are generally correctly identified by the method (van Diedenhoven, Ackerman, et al., 2016). The ice properties inferred from polarized reflectances pertain to the cloud top, down to where the optical depth is approximately unity (van Diedenhoven, Cairns, et al., 2012).

To compute the LUT, a doubling-adding radiative transfer model (De Haan et al., 1987) is used. A rough ocean surface (Cox & Munk, 1956) is assumed using a wind speed of 4 m/s. However, we constrain the results to optically thick clouds ( $\tau > 5$ ) for which the surface influence is minimal, since variation of wind speed over ocean and land surface reflection is not accounted for and this may influence the results for thin clouds. Ice optical properties are calculated using the code of Macke et al. (1996) which is based on the geometric optics (GO) approximation. Only cases with retrieved effective radii larger than  $5 \mu\text{m}$  are included. The GO approximation is generally applicable in the shortwave to compact crystals with such low effective radii although its accuracy decreases with aspect ratio increasingly deviating from unity (Bi et al., 2014; Um & McFarquhar, 2015). Since a weak Rayleigh scattering signal is affecting the polarized reflectances at 865 nm (Hioki et al., 2016), we augmented the LUT with calculations at two additional cloud top pressures, yielding calculations at 378, 286, and 182 hPa. For each observation, the LUT is linearly interpolated or extrapolated to the cloud top pressure obtained from the collocated MODIS Collection 6 (C6) data set (Platnick et al., 2017). This adaptation of the method was found to slightly reduce the vertical variation of results but had little effect qualitatively.

The method is applied to multiangle measurements obtained by POLDER in 2007. Here, we use the combined POLDER-MODIS data set supplied by the ICARE Data and Services Center that includes cloud optical thicknesses, effective radii, cloud top pressures, and temperatures retrieved by MODIS-Aqua (Platnick et al., 2017), averaged over the  $6 \times 6 \text{ km}^2$  pixels of POLDER (Riedi et al., 2010). In addition, the data set includes the cloud thermodynamic phase product obtained from combined POLDER and MODIS information (Riedi et al., 2010). The instrument collects a maximum of 15 different viewing angles for each pixel of about  $6 \times 6 \text{ km}^2$ . Only data with more than five observations within the scattering angle range  $125^\circ$ – $150^\circ$  are selected. Furthermore, only clouds with cloud top temperatures below 273 K and with combined MODIS and POLDER cloud phase flag indicating confident ice (index defined by

Riedi et al., 2010, greater than 150) are selected. We noticed that on occasion the measurements showed clear signs of polarized cloud bow signals, despite these selection criteria. The liquid index was therefore calculated from the polarized reflectances, as described by van Diedenhoven, Fridlind, et al. (2012), and only measurements with liquid index values below 0.3 were considered. Since the polarized reflectances are mainly determined by single backscattering events occurring within the top first optical depth of the cloud layers, these criteria essentially ensure exclusion of observations that have water drops at the tops of clouds anywhere in the instrument footprint.

Effects caused by time differences between measurements at different viewing angles and different polarization angles, subpixel inhomogeneity, and possible other causes may cause substantial variation of polarized reflectances with scattering angle that are not associated with variations in ice crystal shape. These artifacts are expected to lead to a large value of the RRMSD. We filter out data with large RRMSD as described in Appendix A, leading to exclusion of about 25% of the retrievals. Retrievals often lead to distortion parameters at the maximum value of 0.7. However, since polarized reflectances nearly asymptote at such large distortion values (Macke et al., 1996), these situations generally still lead to a good fit with the data and thus low RRMSD. The tendency to retrieve maximum distortion is consistent with previous findings using POLDER data (Hioki et al., 2016).

Previous polarimetric and lidar observations indicate that optically thick cloud layers containing detectable oriented crystals are rare at temperatures below 235 K but quite prevalent at temperatures higher than 235 K (Bréon & Dubrulle, 2004; Zhou et al., 2012). However, the fraction of crystals within these layers that are oriented is estimated to be generally much lower than 1%, and the effect on polarimetric measurements is generally weak. Furthermore, only measurements at scattering geometries within about 1° of the glint angle are affected, which are relatively rare. Moreover, occasional strong specular reflection signals from oriented crystals are expected to lead to large RRMSD values and thus to exclusion from our sample. In summary, it is unlikely that not explicitly accounting for oriented crystals substantially affects our results.

MODIS C6 retrievals (Platnick et al., 2017) of cloud optical thickness, effective radius, cloud top pressure, and temperature are averaged over POLDER footprints, as described by Riedi et al. (2010). Here, effective radius  $r_e$  is defined as (Foot, 1988)

$$r_e = \frac{3}{4} \frac{V_t}{A_t}, \quad (1)$$

where  $V_t$  and  $A_t$  are the total volume and total projected area of the ice crystal population, respectively. Since the single scattering albedo of ice cloud layer at a given wavelength in the shortwave infrared is robustly related to  $r_e$  as defined by equation 1,  $r_e$  can be inferred from total reflectance measurements in the shortwave infrared. For the retrieval of effective radius, the MODIS band located at 2.13  $\mu\text{m}$  is used. Because of the absorption, the reflected light is emerging only from the top of the cloud. Hence, the inferred  $r_e$  represents the effective radius of ice crystals within the first two optical depths integrated from cloud top, while the physical depth within cloud top to which the retrieved  $r_e$  pertains ranges from about 0.5 to 3 km depending on the extinction at cloud top (van Diedenhoven, Fridlind, et al., 2016). The MODIS algorithm assumes an optical model based on rough aggregates of columns with an average component aspect ratio of about 0.67 and asymmetry parameter at 865 nm of  $g_{C6} = 0.754$  (Fu, 2007; Yang et al., 2015). The applied roughness parameter  $\sigma^2$  as defined by Yang, Kattawar, et al. (2008) is equal to 0.5, which is equivalent to a distortion, as used in this paper, of 0.71 (Geogdzhayev & van Diedenhoven, 2016; Neshyba et al., 2013). Uncertainties in pixel-level effective radii are dominated by radiometric uncertainties and uncertainties in asymmetry parameter, while the contribution of uncertainties in particle size distribution is relatively small (Platnick et al., 2017). A 5% uncertainty in  $g$  will lead to about 15% uncertainty in  $r_e$ , and a total uncertainty in  $r_e$  can be estimated to be about 25% (or generally about 8  $\mu\text{m}$ ) (Platnick et al., 2017). Here, average values are reported of at least 1,000 POLDER pixels, and most random errors can be assumed to average out. Local biases because of, for example, subpixel inhomogeneity (Fauchez et al., 2018; Zhang et al., 2016) cannot be ruled out. If we take as a measure for inhomogeneity the standard deviation of MODIS cloud optical thicknesses within a POLDER footprint, as provided in the combined POLDER-MODIS data set, relative to the corresponding mean optical thickness, we find that inhomogeneity increases with mean optical thickness but do not find any other apparent correlation with inhomogeneity and retrieved ice properties.

**Table 1**  
Total Number of Data Points and Averaged Values of Retrieved Parameters  
(Standard Deviations in Brackets)

Parameter	All	Land	Ocean
Number	84,702,614	24,575,002	60,127,612
Cloud top temperature (K)	229 (11.6)	227 (11.3)	227 (11.9)
Asymmetry parameter	0.742 (0.0384)	0.746 (0.0425)	0.740 (0.0364)
Aspect ratio	0.497 (0.196)	0.487 (0.202)	0.503 (0.192)
Column fraction (%)	10.4	10.2	10.5
Distortion	0.621 (0.177)	0.598 (0.204)	0.630 (0.160)
Effective radius ( $\mu\text{m}$ )	34.7 (8.97)	32.2 (9.43)	35.8 (8.56)

Further, we find that the RRMSD obtained as part of the retrieval of aspect ratio and distortion parameters (see Appendix A) increases systematically with inhomogeneity, which implies that the applied filter on RRMSD also partly serves as a filter on inhomogeneity.

To correct the C6 retrievals for the assumption of an invariant asymmetry parameter, average optical thickness and effective radius retrieved for a given POLDER pixel are divided and multiplied, respectively, by the factor  $(1 - g_P)/(1 - g_{C6})$ , where  $g_P$  is the asymmetry parameter at 865 nm retrieved from the POLDER observations (van Diedenhoven, Fridlind, et al., 2014). This scaling factor applied to the optical thickness conserves the scaled optical thickness  $\tau(1 - g)$  and thus leads to similar visible reflectance with changing  $g$  (Stephens et al., 2001). The extinction

efficiency for cloud ice crystals is close to 2 at all solar wavelengths, so the total optical thickness  $\tau$  does not vary with wavelength and the same scaling factor is applied to  $\tau$  in the shortwave. However, in the shortwave infrared, the reflectance is also affected by ice absorption, and the absorption optical thickness  $\tau(1 - \omega)$  needs to be conserved for a change in  $g$  (Twomey & Bohren, 1980). This implies  $(1 - \omega)$  needs to be scaled by the inverse of the scaling applied to  $\tau$ . Considering ice is relatively weakly absorbing at 2.13  $\mu\text{m}$ ,  $(1 - \omega)$  can be assumed to be approximately linearly related to  $r_e$  (van Diedenhoven, Ackerman, et al., 2014; Twomey & Bohren, 1980). Thus,  $\tau(1 - \omega)$  is approximately conserved when  $\tau \times r_e$  is conserved, implying  $r_e$  is properly scaled through *division* by the factor  $(1 - g_P)/(1 - g_{C6})$ , where  $g_P$  and  $g_{C6}$  represent the asymmetry parameters at 865 nm. This scaling is also consistent with the observation that ice water paths derived from the product of retrieved optical thickness and effective radius are not substantially sensitive to the assumed ice optical model (Ding et al., 2017; Yang, Hong, et al., 2008). Other scaling methods have been proposed but generally yield less accurate results when tested on real observations (Ding et al., 2017).

### 3. Results

#### 3.1. Global Statistics and Vertical Variation

Global statistics of retrieved cloud top temperature, effective radius, asymmetry parameter, distortion parameter, component aspect ratio, and the percentage of pixels for which a columnar crystal geometry is inferred (denoted column fraction hereafter) are listed in Table 1 for optically thick clouds (with  $\tau > 5$ ) separated between cases over land and ocean and separated by various latitude ranges and seasons in Table 2. Global maps are provided in Figure 1 and are obtained by averaging all available data within 5° gridboxes. For most parameters, arithmetic averages and standard deviations are reported. However, as geometric averages of aspect ratios better represent the radiative properties of ice crystal ensembles (van Diedenhoven, Ackerman, et al., 2016), we present geometric averages for aspect ratios. The corresponding standard deviations are calculated as  $\mu(1 - 1/\sigma_{\text{SDF}})$ , where  $\mu$  represents the geometric average and  $\sigma_{\text{SDF}}$  is the geometric standard deviation factor. As discussed in section 2, optical thicknesses and effective radii from the MODIS C6 product are corrected for the difference between the asymmetry parameter assumed in the C6 algorithm and the values retrieved here. Results for uncorrected  $r_e$  are shown in supporting information Figure S1. Since the total number of retrievals is large (over 84 million, see Table 1) and only averages with at least 1,000 values are considered, essentially all variations of mean parameters discussed in this paper are statistically significant given their associated standard errors.

As seen in Table 1, average  $r_e$  values are generally close to 35  $\mu\text{m}$ , while component aspect ratios, distortion parameters, and asymmetry parameters are near 0.50, 0.62, and 0.74, respectively. About 90% of the measurements indicate that plate-like crystal components are dominant. The globally averaged asymmetry parameter is consistent with previous global assessments and with the ice model assumed for MODIS C6 retrievals (Platnick et al., 2017). The maps shown in Figure 1 suggest some latitudinal variation of ice crystal properties, as well as contrasts between land and ocean. Note, however, that part of the latitudinal variation in average properties may be attributed to variation in average cloud top temperature (see Figure 1a and Table 2), as further discussed below.

**Table 2**  
As Table 1, But Separated by Location and Season

Parameter	Tropical	Summer	Winter	High latitude
<b>Ocean</b>				
Number	21,917,726	6,077,998	4,835,874	7,530,138
Cloud top temperature (K)	220 (11.6)	231 (7.89)	229 (9.70)	233 (10.3)
Asymmetry parameter	0.737 (0.0361)	0.743 (0.0346)	0.736 (0.0343)	0.749 (0.0410)
Aspect ratio	0.505 (0.209)	0.493 (0.186)	0.540 (0.162)	0.457 (0.179)
Column fraction (%)	10.9	13.3	5.85	11.3
Distortion	0.645 (0.140)	0.629 (0.155)	0.625 (0.178)	0.597 (0.202)
Effective radius ( $\mu\text{m}$ )	37.0 (9.37)	40.0 (10.6)	35.8 (9.81)	38.3 (12.2)
<b>Land</b>				
Number	8,442,930	758,494	2,536,672	5,034,920
Cloud top temperature (K)	221 (12.9)	231 (10.1)	232 (11.9)	235 (11.7)
Asymmetry parameter	0.744 (0.0426)	0.747 (0.0434)	0.741 (0.0391)	0.752 (0.0455)
Aspect ratio	0.479 (0.220)	0.490 (0.216)	0.521(0.175)	0.469 (0.186)
Column fraction (%)	11.8	12.9	5.69	9.12
Distortion	0.623 (0.169)	0.602 (0.190)	0.597 (0.211)	0.562 (0.242)
Effective radius ( $\mu\text{m}$ )	33.9 (10.5)	33.4 (11.9)	31.8 (11.4)	32.5 (12.4)

Ice microphysical properties have been previously observed to depend on temperature, among other factors, in laboratory and in situ measurements (Bailey & Hallett, 2004, 2009), and equivalently on cloud top height or temperature in remote sensing surveys (van Diedenhoven, Fridlind, et al., 2016; Yuan & Li, 2010). In Figures 2 and 3, we evaluate our results over ocean and land, respectively, as a function of cloud top temperature for high ( $>60^\circ$ ) and tropical ( $30^\circ\text{S}$  to  $30^\circ\text{N}$ ) latitudes and for midlatitudes separated between summer and winter months. Statistics for the profiles are gathered within 2-K-wide temperature bins. Clouds with tops colder than the homogeneous freezing level at about 235 K can be interpreted as optically thick cold cirrus and convective clouds, while warmer clouds can be interpreted as warm cirrus, glaciated (alto) stratus, or growing or decaying (transient) convection or “terminal” cumulus congestus (van Diedenhoven, Fridlind, et al., 2012; Luo et al., 2009).

At middle and high latitudes most thick ice clouds are seen around the level of homogeneous freezing, while numbers quickly drop at colder levels. In the tropics, the maximum number of thick ice clouds occurs at somewhat lower cloud top temperatures, and a substantial number of clouds with top temperatures down to 190 K are observed. Figures 2b and 3b show that, for most cloud top temperatures,  $r_e$  is generally largest in the tropics and during midlatitude summer, especially over ocean. Over ocean, average  $r_e$  values are generally around 25–35  $\mu\text{m}$  for cold cloud tops, increase with increasing cloud top temperatures up to about 246–248 K, and decrease again for warmer cloud tops. Over land,  $r_e$  are generally 2–10  $\mu\text{m}$  smaller than over ocean with the largest contrast seen for warm cloud tops. Furthermore, the transition between decreasing and increasing  $r_e$  with temperature occurs at a cloud top temperature that is about 2–5 K lower than over ocean. The robust filtering for liquid-phase cloud tops provided by the polarimetry precludes this transition resulting from a thermodynamic phase transition as previously suggested (Yuan et al., 2010).

To derive a plausible explanation of the observed vertical variation of cloud top effective radius, we consider that in the case that cloud top ice crystals have been formed in situ, their growth is limited in part by the level of supersaturation over ice and the ice saturation vapor pressure (Pruppacher & Klett, 1997). The single particle growth rate at a given temperature and pressure can be expressed as (Pruppacher & Klett, 1997)

$$\frac{dm}{dt} \approx 4\pi f_c G (S_i - 1) D_{\text{max}}, \quad (2)$$

where  $f_c$  is the nondimensional capacitance shape factor with respect to maximum dimension  $D_{\text{max}}$  and  $S_i$  is the saturation ratio with respect to ice. The function  $G$  accounts for thermal and vapor diffusion processes depending on temperature  $T$  and pressure  $P$  and can be expressed as (Pruppacher & Klett, 1997)

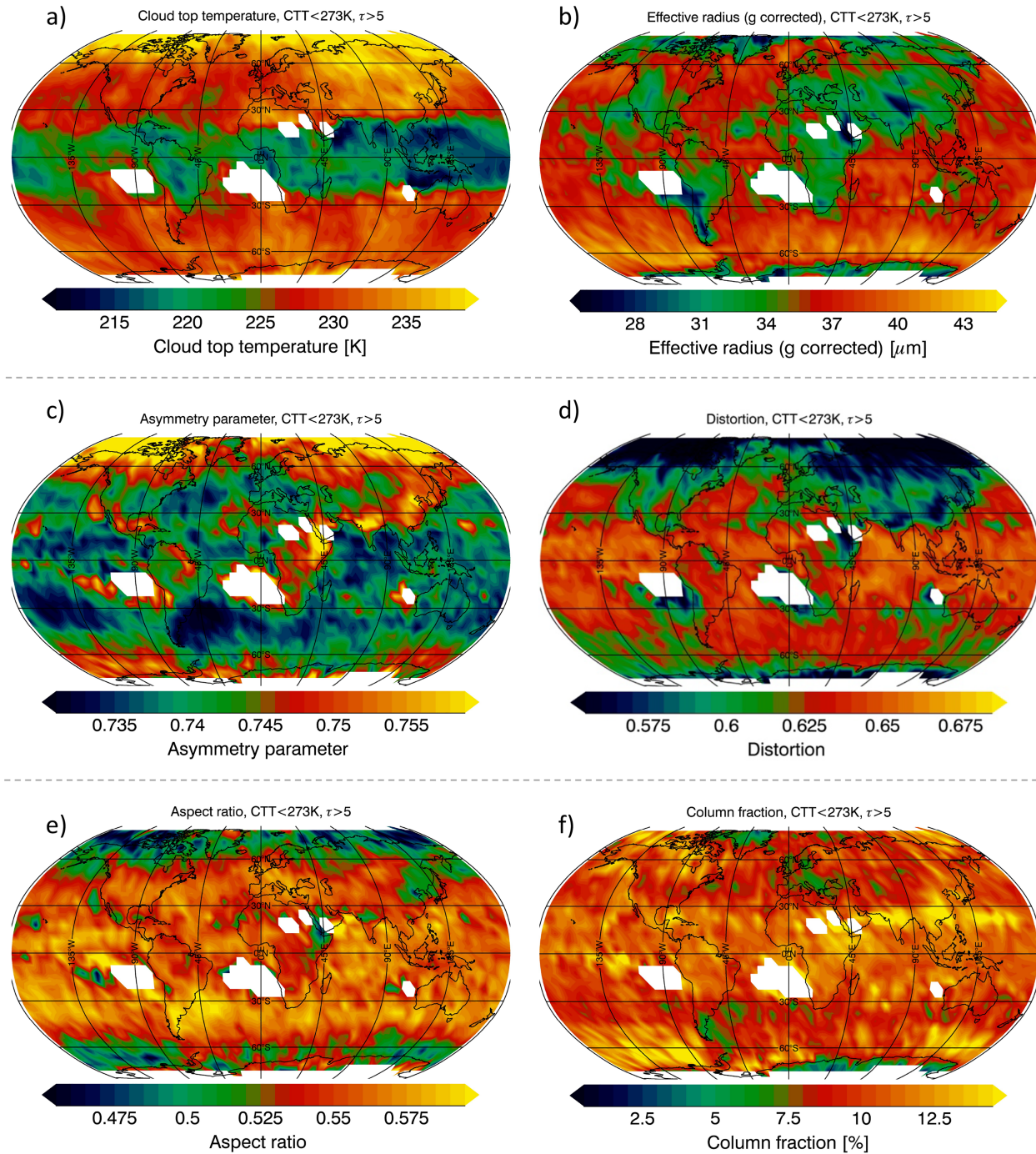


**Figure 1.** Global distributions of average retrieved cloud top temperature (a), ice effective radius (b), asymmetry parameter (c), distortion (d), aspect ratio of crystal components (e), and column fraction (f) derived from MODIS and POLDER measurements from 2007. Effective radii are obtained from MODIS C6 product and corrected for the assumption of an invariant ice optical model, using the retrieved asymmetry parameter values. Only ice clouds with a cloud top temperature (CTT) below 273 K and an optical thickness ( $\tau$ ) greater than 5 are included.

$$G(T, P) \approx \frac{1}{\frac{R_w T}{e_{\text{sat},i} D_v} + \frac{L_s}{k_a T} \left( \frac{L_s}{R_w T} - 1 \right)}, \quad (3)$$

where  $e_{\text{sat},i}$  is the saturation vapor pressure over ice,  $D_v$  the diffusivity of water vapor in air,  $L_s$  the latent heat of sublimation,  $k_a$  the thermal conductivity of air, and  $R_w$  the gas constant for water vapor. We

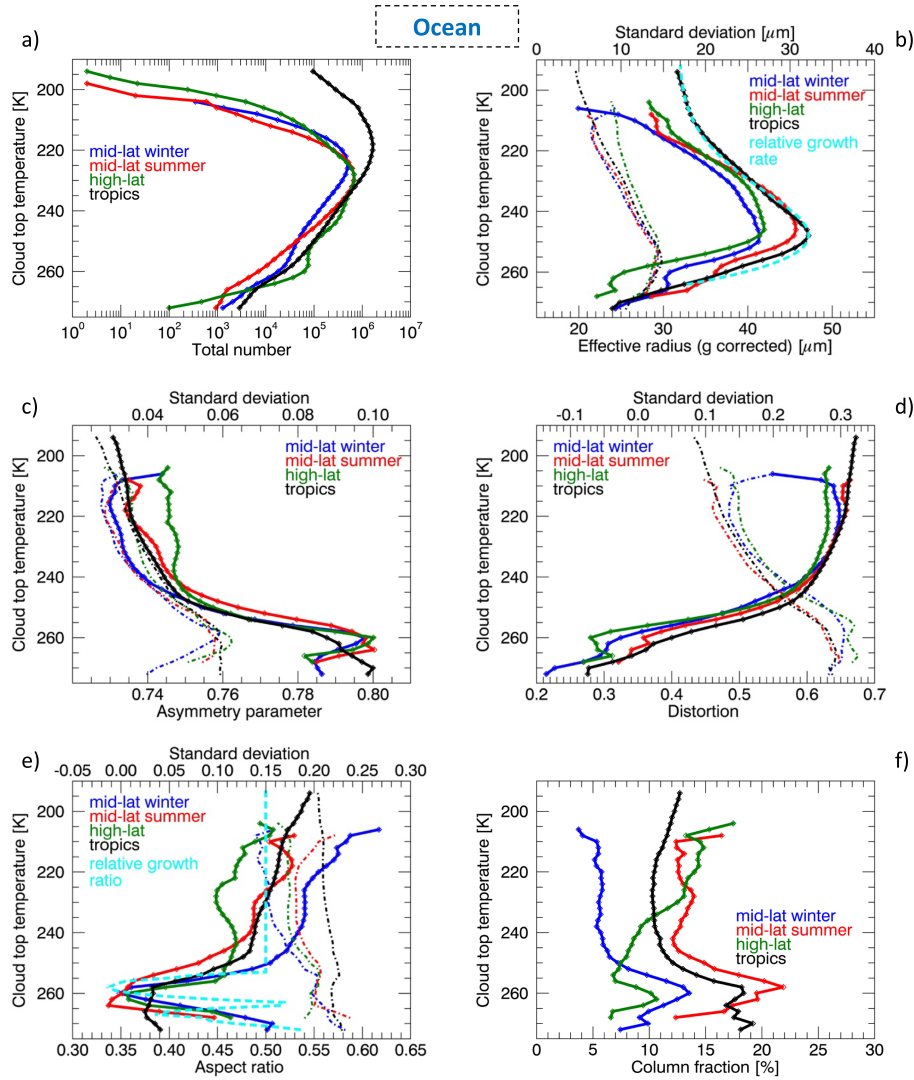


**Figure 2.** Number of observations (a) and statistics of ice effective radius (b), asymmetry parameter (c), distortion (d), aspect ratio of crystal components (e), and column fraction (f) as a function of cloud top temperature for ice clouds over ocean. Solid lines show average values (bottom axis), while dash-dotted lines show the standard deviations (top axis). Colors indicate regions and seasons for which averages are taken. The cyan dashed line in panel (b) represents the estimated relative ice growth rate with  $S_i(T)$  given by equation (10) and  $f_{ws}$  set to 0.92, scaled, and in arbitrary units as discussed in the text. The cyan dashed line in panel (e) shows the scaled relative inherent ice growth ratio, as defined in the text.

take  $e_{sat,i}$  from Bohren and Albrecht (1998) and  $k_a$  and  $D_v$  from Pruppacher and Klett (1997) (omitting gas kinetic effects). To relate pressure to temperature, we use the U.S. standard tropical atmosphere. We omit the small temperature dependence of  $L_s$ , which is held constant at  $2.834 \cdot 10^6 \text{ J kg}^{-1}$ . Furthermore, note that equation (3) omits complications that depend on particle size: ventilation (e.g., Pruppacher & Klett, 1997), gas kinetic effects (e.g., Pruppacher & Klett, 1997), solute and curvature corrections (e.g., Pruppacher & Klett, 1997), and radiative heating of particles (e.g., Barkstrom, 1978). To derive the growth rate of total, particle-size-distribution-integrated mass, or the more commonly used total mass mixing ratio  $q$  defined as total mass per unit air mass, equation (3) is integrated over the particle size distribution, yielding

$$\frac{dq}{dt} \approx 4\pi f_c G (S_i - 1) M_n, \quad (4)$$

where  $M_n$  is the  $n$ th moment of the particle size distribution in terms of  $D_{max}$ . Using the chain rule, we can relate effective radius growth rate to mass mixing ratio growth rate by

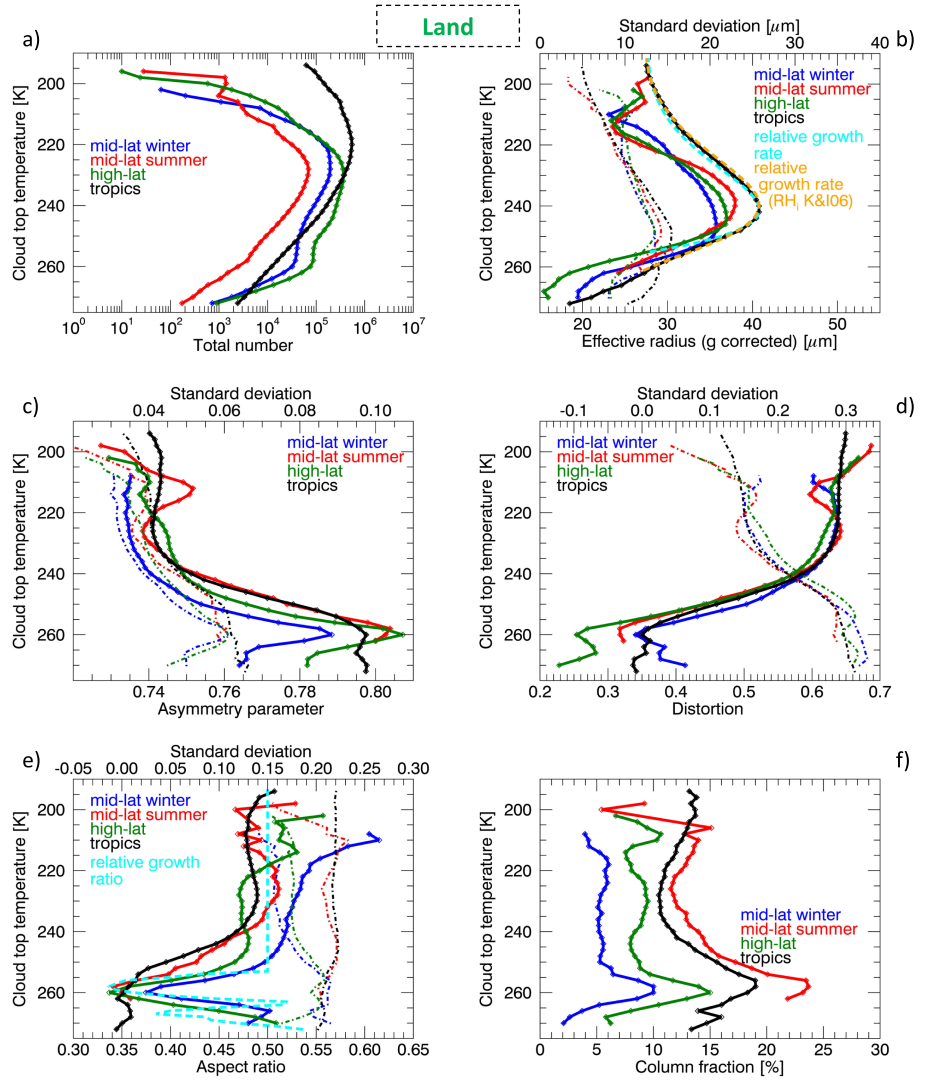


**Figure 3.** As Figure 2, but for clouds over land. The cyan and orange dashed lines in panel (b) represent the scaled relative ice growth rates calculated with  $S_i(T)$  given by equation (10) and  $f_{iws}$  set to 0.84 and using the relative humidity parameterized by Korolev and Isaac (2006), respectively.

$$\frac{dr_e}{dt} = \frac{dr_e}{dq} \frac{dq}{dt} \quad (5)$$

As shown by equation (1), the effective radius is proportional to the ratio of total ice mass to total ice projected area. Assuming that mass and projected area of individual ice crystals can be related to their maximum dimension via power laws with exponents  $\gamma$  and  $\sigma$ , respectively (Mitchell, 1996),  $r_e$  is proportional to the ratio of the moments  $M_\gamma$  and  $M_\sigma$ ; that is,

$$r_e \sim \frac{M_\gamma}{M_\sigma} \quad (6)$$

Furthermore, we have

$$q \sim M_\gamma, \quad (7)$$

which implies

$$\frac{dr_e}{dq} \sim \frac{1}{M_\sigma}. \quad (8)$$

Finally, equations (4) to (8) lead to

$$\frac{dr_e}{dt} \sim G(S_i - 1)M_{-\sigma}. \quad (9)$$

Equation (9) indicates that the effective radius growth rate depends on particle size itself through the multiplication by the moment  $M_{-\sigma}$ , where  $\sigma$  ranges from about 1.4 to 2 for typical cloud ice crystal habits (Fridlind et al., 2016; Heymsfield et al., 2003; Mitchell, 1996; Schmitt et al., 2010). However, here we focus on the temperature dependence of the estimated *relative* ice growth, by assuming that the size dependence of the effective radius growth rate expressed by equation (9) is independent of temperature and computing  $G(S_i - 1)$  as a function of temperature and then normalizing the result by its largest value. The size dependency of equation (9) can be interpreted as a feedback, where small crystals grow more efficient in terms of  $r_e$  than large crystals. Since we are focusing on relative ice growth rates, this size feedback has a negligible effect on the temperature dependence of the relative effective radius growth rate. Note, however, that the temperature dependence of the relative effective radius growth rate may be affected by a substantial temperature dependence of  $\sigma$ , although no reliable information on the variation of  $\sigma$  with cloud top temperature is available to our knowledge.

At water saturation, growth rates derived from equations (2), (4), and (9) increase with decreasing temperatures between 273 and about 255 K and decrease for lower temperatures (Fukuta & Takahashi, 1999; Jensen et al., 2017; Pruppacher & Klett, 1997). However, supersaturation levels in ice clouds are generally below that corresponding to liquid saturation but increase with decreasing temperatures (Korolev & Isaac, 2006). The temperature at which the transition in growth rates occurs depends on the *profile* of relative humidity over ice and not its absolute values. To illustrate this dependence, we estimate vapor deposition effective radius growth rates from equation (9) (relative to its largest value) (Pruppacher & Klett, 1997) and assume a relative humidity with respect to ice profile corresponding to water saturation arbitrarily scaled by a constant fraction  $f_{ws}$ ; that is,

$$S_i(T) \approx f_{ws} \frac{e_{sat,w}(T)}{e_{sat,i}(T)}, \quad (10)$$

where  $e_{sat,w}$  is the saturation vapor pressure over liquid water (Bohren & Albrecht, 1998). Setting  $f_{ws}$  to 0.92 and 0.84 for conditions over ocean and land results in relative growth rate curves shown in cyan in Figures 2b and 3b, respectively. Note that only relative ice growth rates are considered for  $S_i(T) > 1$  and the curves shown in Figures 2a and 3a are scaled so that their values at 220 K and their maximum values match the corresponding  $r_e$  values of the observed tropical profiles over ocean and land, respectively, thus representing the scaled relative temperature dependence of ice growth rates. Figures 2b and 3b show that the estimated relative growth rates follow the observed  $r_e$  temperature trends remarkably well. The lower value of  $f_{ws}$  needed over land may be consistent with generally dryer conditions over land compared to ocean, which may also explain the smaller  $r_e$  over land, as well as during winter and at high latitudes. Alternatively, over land, we can assume a parameterization of the relative humidity in ice clouds based on observations within continental deep ice clouds provided by Korolev and Isaac (2006), which leads to relative growth rates profiles shown by the orange dashed curve in Figure 3b that arguably compares even better to the  $r_e$  profiles over land. Note that no maximum in growth rates occurs when assuming supersaturation to be constant with temperature. The effective radius of the ice particle size distribution in a volume of air is determined by its history of ice formation, growth by various mechanisms, and transport of particles into and out of the volume by sedimentation and turbulent mixing. The finding that the temperature dependence of the relative growth rate is similar to the temperature dependence of effective radius may suggest that ice particle distributions observed at cloud top have generally been subjected to depositional growth for a uniform amount of time at average conditions similar to the observed cloud top. However, such a conclusion is somewhat surprising as, within updrafts,  $r_e$  at cloud top is expected to be an integral manifestation of processes at lower levels, as far down as the liquid phase. Aside we note that the slight increase of  $r_e$  near

265 K over ocean, especially in midlatitude winter and at high latitudes, is consistent with laboratory measurements showing a local increase in growth rate at those temperatures (Fukuta & Takahashi, 1999; Jensen et al., 2017). Over land,  $r_e$  quite abruptly increases with decreasing temperatures below about 225 K at middle and high latitudes, which is also observed using Atmospheric Infrared Sounder measurements and may be consistent with overshooting convection (Kahn et al., 2018).

Figures 2 and 3 indicate that cloud top temperature trends of asymmetry parameters, distortion values, and aspect ratios are qualitatively similar over ocean and land. Asymmetry parameters are generally around 0.72 to 0.75 for cloud tops colder than 235 K. For warmer clouds, there is a pronounced increase of the asymmetry parameter with temperature that mainly results from the decrease of distortion with temperature. Greater prevalence of low crystal distortion at warm conditions is consistent with halos seen more often in warm ice clouds (Bailey & Hallett, 2004; van Diedenhoven, 2014) and with the correlation between crystal complexity or surface roughness and growth rate recently observed in cloud chamber and laboratory studies (Schnaiter et al., 2016; Voigtländer et al., 2018). The observed aspect ratios are generally within a range of 0.35 to 0.6 with a noteworthy minimum apparent at around 260 K. As shown in Figures 2d and 3d, this minimum is largely consistent with the temperature dependence of the relative inherent growth ratios for plate-like crystals that are used in adaptive habit microphysics schemes that aim to simulate crystal aspect ratios (Hashino & Tripoli, 2011; Jensen et al., 2017). The relative inherent ice growth ratios shown in Figures 2e and 3e are derived from Chen and Lamb (1994), with growth ratios values for temperatures below 253 K set to 0.8, as suggested by Hashino and Tripoli (2011) for plates. Furthermore, growth ratios around 265 K with values larger than unity are inverted to be consistent with the definition of particle aspect ratio used here. For the sake of comparison, the relative inherent growth ratios curves shown in Figures 2e and 3e are scaled so that the values at 200 K are 0.5 and the minimum values are equal to the lowest observed mean aspect ratio. These relative growth rates indicate that particles with relatively thin components are expected from vapor growth processes at around 260 K, consistent with the minimum in retrieved component aspect ratio. Note that the retrievals indicate that crystal components with plate-like geometries dominate at all temperatures (Figures 2f and 3f). This finding is largely consistent with theory and observations for temperatures above 233 K (Bailey & Hallett, 2009; Hashino & Tripoli, 2007), although the slight increase in column fraction around 260 K appears to be inconsistent with the expected increase in thin plates. Furthermore, at conditions colder than 233 K and at sufficiently high supersaturations, columnar habits are generally assumed to be more prevalent than plate-like crystals (Bailey & Hallett, 2004; Lawson et al., 2019). However, at such temperatures, crystals are generally polycrystalline and often classified as irregular crystals, especially in thick ice clouds, making firm conclusions on the dominating shapes of the crystal components from in situ images to be effectively impossible (Bailey & Hallett, 2009; Lawson et al., 2019). Note that, while our results indicate that plate-like crystal components dominate, the average aspect ratio of about 0.5 is consistent with thick plates, which are often confused with short columns and may also be components of “budding rosettes” (Bailey & Hallett, 2004, 2009). Interestingly, column fractions are about 10% larger for midlatitude summer and in the tropics. We speculate that this greater prevalence may be related to the more humid conditions for those samples, which is more conducive to formation of columnar crystal components (Bailey & Hallett, 2004).

### 3.2. Covariation of Effective Radius, Shape, and Asymmetry Parameter

The covariation of effective radius, ice crystal component aspect ratio, distortion, and asymmetry parameter for cold and warm clouds over ocean and land is shown in Figures 4 and 5, respectively. Here, statistics of properties as a function of  $r_e$  are calculated in 2- $\mu\text{m}$ -wide bins. Figures 4 and 5 reveal that generally  $g$  strongly decreases with increasing  $r_e$ , perhaps unexpectedly, whereas distortion and aspect ratio are found to increase. Furthermore, asymmetry parameters for small  $r_e$  are generally larger for clouds warmer than 235 K, mainly because the increase of distortion parameter with  $r_e$  is weaker for warmer clouds. Although most past assessments have concluded that ice population asymmetry parameters weakly *increase* or are largely constant with increasing  $r_e$ , the pronounced covariations of distortion, aspect ratio, and asymmetry parameter found here are consistent with recent in situ and laboratory measurements in several ways. First, Schmitt et al. (2016) concluded that the smallest crystals observed in situ are generally relatively simple and pristine until a transition to more complex crystals occurs at maximum dimensions of around 100  $\mu\text{m}$  for the coldest clouds observed, increasing to 200  $\mu\text{m}$  at temperatures near the melting level. Assuming

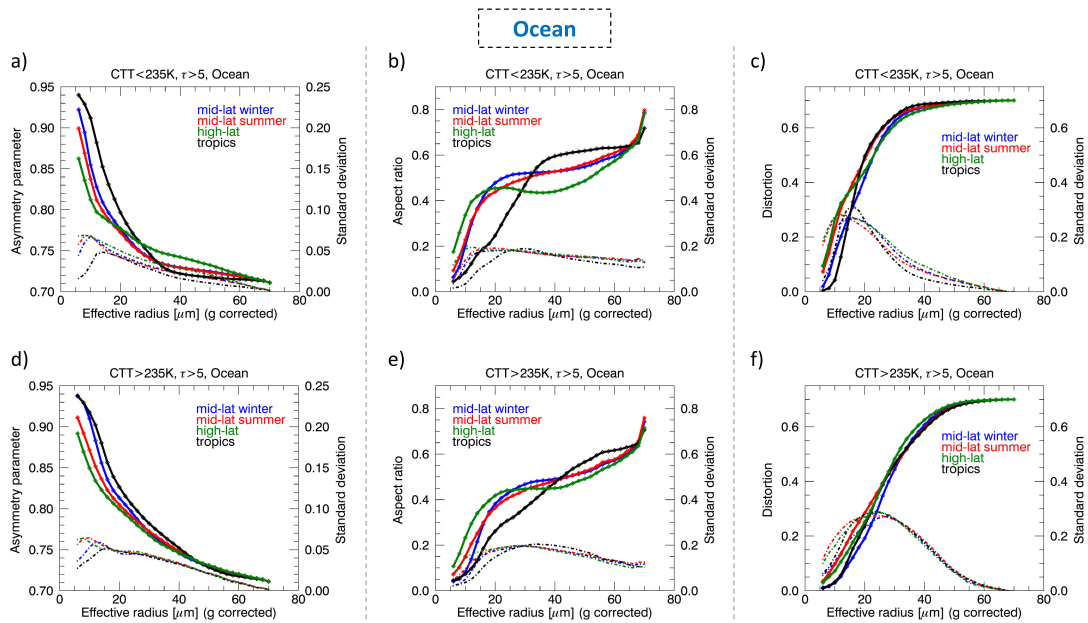


**Figure 4.** Statistics of the asymmetry parameters (a, d), aspect ratios (b, e), and distortion parameters (c, f) as a function of effective radius corrected for retrieved asymmetry parameter for clouds over ocean. Top row (a–c) and bottom row (d–f) show results for cloud top temperatures (CTT) lower and higher, respectively, than 235 K. Solid lines show average values (left axes), while dashed-dotted lines show the standard deviations (right axes). Colors indicate regions and seasons for which averages are taken.

hexagonal plates, these complexity transition sizes correspond to effective radii of about 25 and 50  $\mu\text{m}$  for the coldest and warmest conditions, respectively, roughly consistent with the transitions to severely distorted crystal populations found here for clouds colder and warmer than 235 K, respectively. Second, simulations by Um and McFarquhar (2009) indicate that, for particles with a fixed mass but increasing complexity,  $g$  and projected area both decrease, leading to a negative correlation between  $g$  and  $r_e$ , consistent with our results. Third, the same simulations by Um and McFarquhar (2009) also indicate that particle components increasingly overlap as complexity increases, thereby effectively increasing averaged component aspect ratios closer to unity, leading to a positive relationship between component aspect ratio

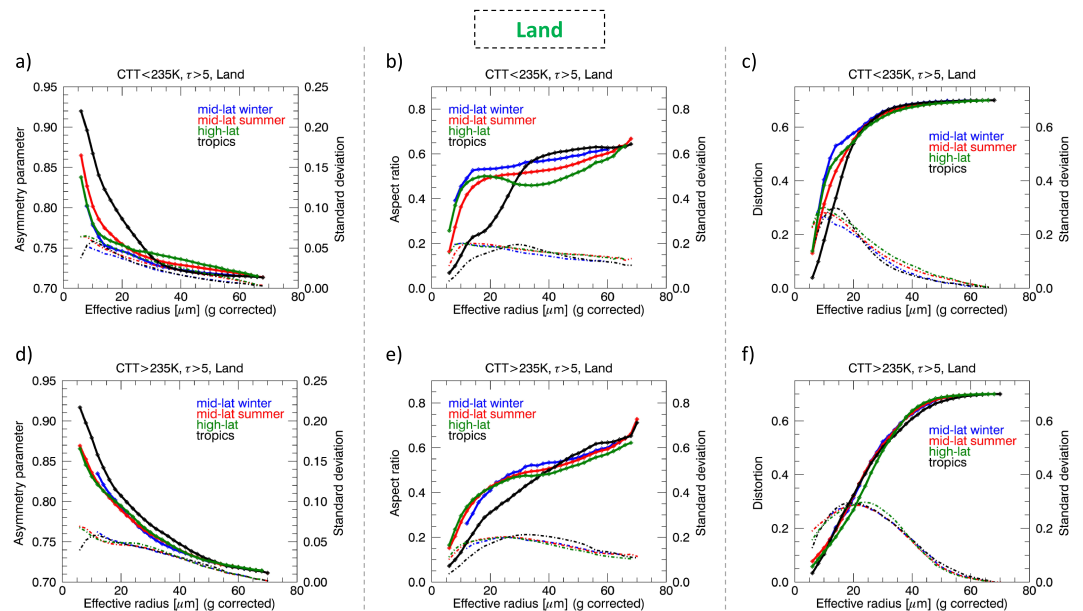


**Figure 5.** Same as Figure 4 but then for clouds over land.

and  $r_e$ , as observed. Fourth, for ensembles of crystals with varying aspect ratios but the same ice water content, the mean projected area for those ensembles with lower mean aspect ratios will be greater than for those with more compact particles, again leading to a positive relation between aspect ratio and  $r_e$  (see equation (1)). Finally, recent cloud chamber and laboratory studies show strong correlations between ice crystal growth rates and complexity or surface roughness parameters derived from an optical probe (Schnaiter et al., 2016; Voigtländer et al., 2018), consistent with increasing distortion with crystal size.

Note, however, that the retrieval of  $r_e$  is not independent of asymmetry parameter, as  $r_e$  is corrected for retrieved  $g$ . The variation of  $g$  with *uncorrected* C6  $r_e$  is much weaker (see supporting information Figures S4 and S5), which is to be expected because the assumption of a nearly invariant  $g = 0.75$  in the C6 algorithm leads to a positive bias in  $r_e$  when the actual  $g$  is larger and vice versa, smoothing out any negative relationship between  $r_e$  and  $g$ . However, our filtering for goodness of fit, large number of data points, and consistency with in situ and laboratory measurements suggest that the derived relationships between  $r_e$ , aspect ratio, distortion, and asymmetry parameter are robust.

### 3.3. Variation With Optical Thickness

The results presented in sections 3.1 and 3.2 are for averages of all clouds with an optical thickness larger than 5. To investigate how the ice properties vary with cloud optical thickness, we provide averages of the properties in cloud top height and cloud optical thickness bins over ocean and land in Figures 6 and 7, respectively. Different cloud optical thickness ranges may be associated with cloud types (Rossow & Schiffer, 1999; van Diedenhoven, Fridlind, et al., 2012). Figures 6a and 7a show that, over ocean and land, numbers generally decrease with optical thickness and that mean optical thicknesses are around 20 at all cloud top temperatures down to about 220 K below which they sharply increase representing fully developed deep convective systems. In general,  $r_e$  decreases with increasing optical thickness. This may at least be partly explained by the extinction increasing with decreasing  $r_e$  at constant ice water content (Platt, 1997). Interestingly, the increased  $r_e$  at cloud top temperatures around 210 K that was apparent in Figure 3 is observed over both ocean and land and may be associated with overshooting convection as discussed above. In general, the vertical variation of all ice properties is qualitatively similar to those shown in Figures 2 and 3 for all optical thicknesses. However, strength of vertical variation of  $r_e$  decreases with increasing optical thicknesses, while the temperature where the maximum  $r_e$  is observed decreases. An interpretation consistent with the theory presented in section 3.1 is that that cloud tops with higher optical thickness are dryer on average. However, differences in dynamics are likely and warrant future study. In contrast, the vertical variation of ice properties other than  $r_e$  is somewhat weaker at low optical thicknesses. This may be attributable to the observation that  $r_e$  generally increases with decreasing optical thickness and that the greatest variation in ice shape and asymmetry parameter occurs at small  $r_e$  as seen in section 3.2.

### 3.4. Scaled Mass Extinction Coefficients

The systematic variation of asymmetry parameters with cloud top temperature and  $r_e$  has implications for the variability of solar reflectivity for ice clouds with a given ice water path. For a vertically invariant cloud layer with a given ice water path (IWP), the optical thickness is determined by

$$\tau = \text{IWP} \beta_m, \quad (11)$$

where we defined the mass extinction coefficient  $\beta_m$  as (Platt, 1997)

$$\beta_m = \frac{\sigma_e}{W}, \quad (12)$$

where  $\sigma_e$  is the total extinction and  $W$  is the ice water content. Consistent with equation (1),  $r_e$  is expressed as

$$r_e = \frac{3Q_e W}{4 \sigma_e \rho_i}, \quad (13)$$

where  $Q_e$  is the ice extinction efficiency and  $\rho_i$  is the bulk density of ice. From equations (12) and (13), we derive

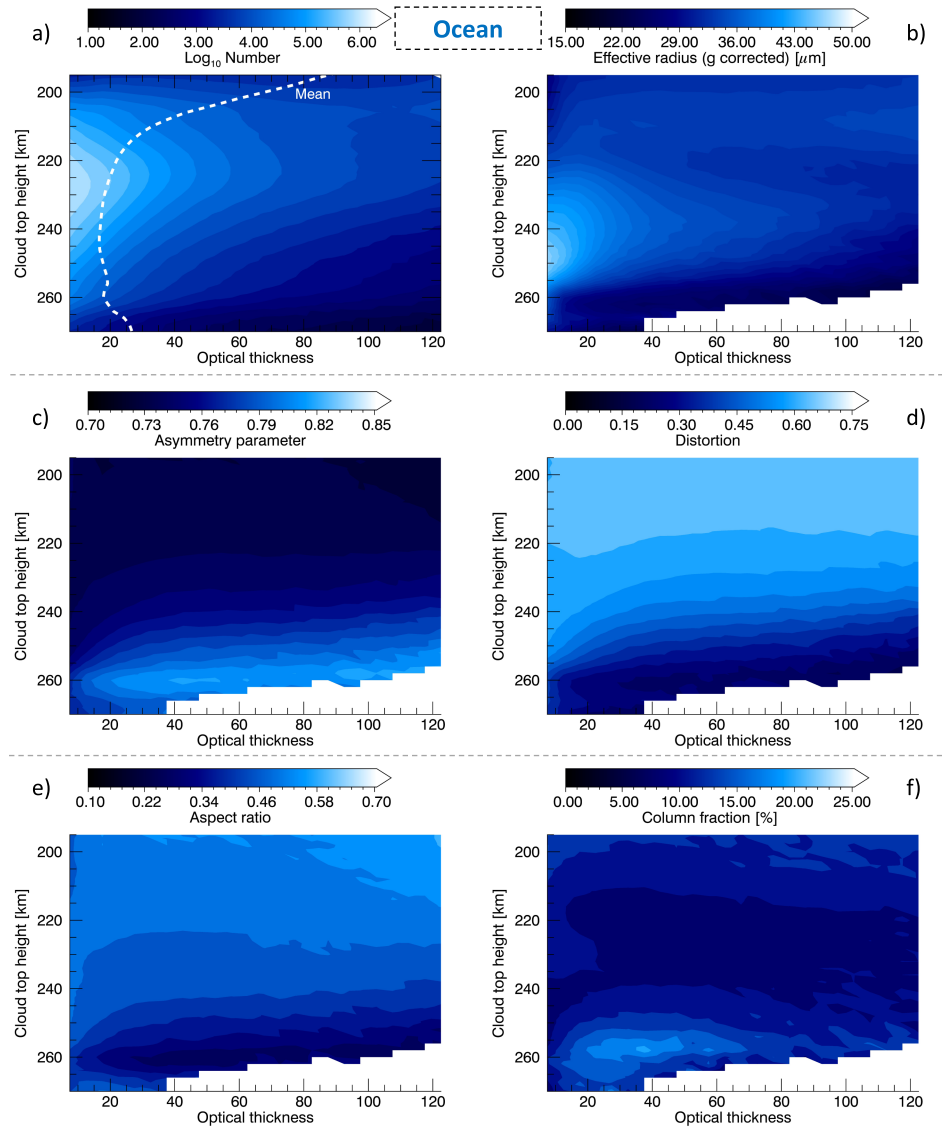


**Figure 6.** Number of observations (a) and average ice effective radius (b), asymmetry parameter (c), distortion (d), aspect ratio of crystal components (e), and column fraction (f) as a function of cloud top temperature and optical thickness for ice clouds over ocean. The dashed line in panel (a) represents the average cloud optical thickness as a function of cloud top temperature.

$$\beta_m \approx \frac{3}{2r_e \rho_i}, \quad (14)$$

where  $Q_e$  is assumed to be equal to 2. Moreover, analogously to the scaled optical thickness  $\tau(1 - g)$  (Stephens et al., 2001), we can define a scaled mass extinction coefficient  $\beta_s$  as

$$\beta_s = \frac{3}{2r_e \rho_i} (1 - g). \quad (15)$$

Thus, the reflectivity of a vertically invariant cloud layer at visible wavelengths is primarily a function of the ice water path and the scaled mass extinction coefficient  $\beta_s$ . Figure 8a shows the variation of derived  $\beta_s$  as a function of cloud top temperature over ocean, indicating that ice cloud tops near 250 K are the least reflective for a given ice water path. Conversely, the coldest and warmest optically thick ice cloud tops considered are similarly reflective for a given ice water path. A similar vertical variation of cloud top  $\beta_s$  is seen over land

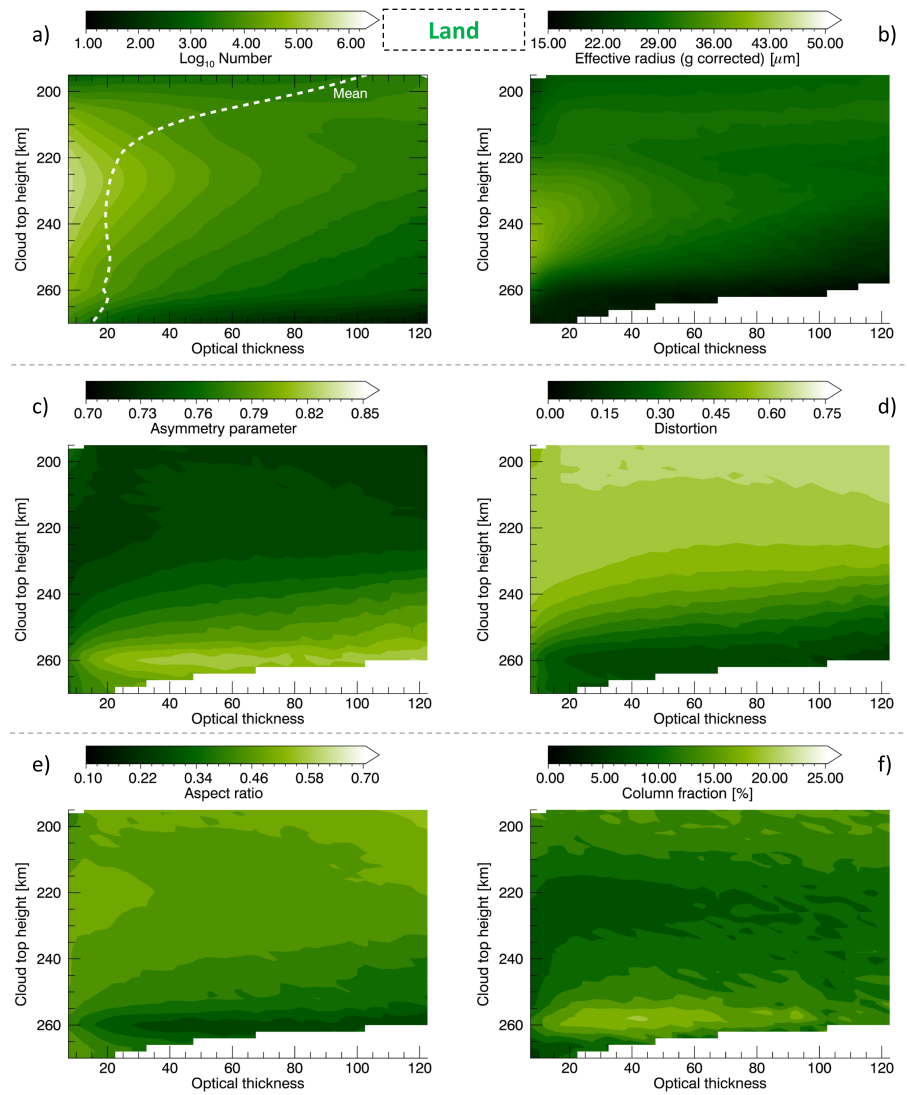


Figure 7. As Figure 6, but for clouds over land.

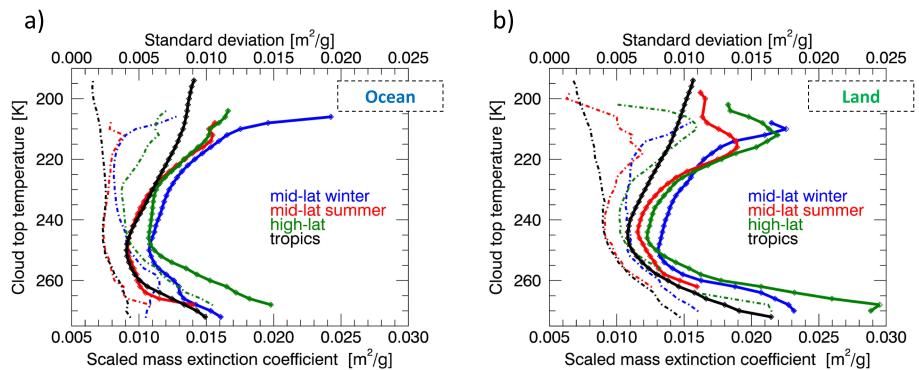
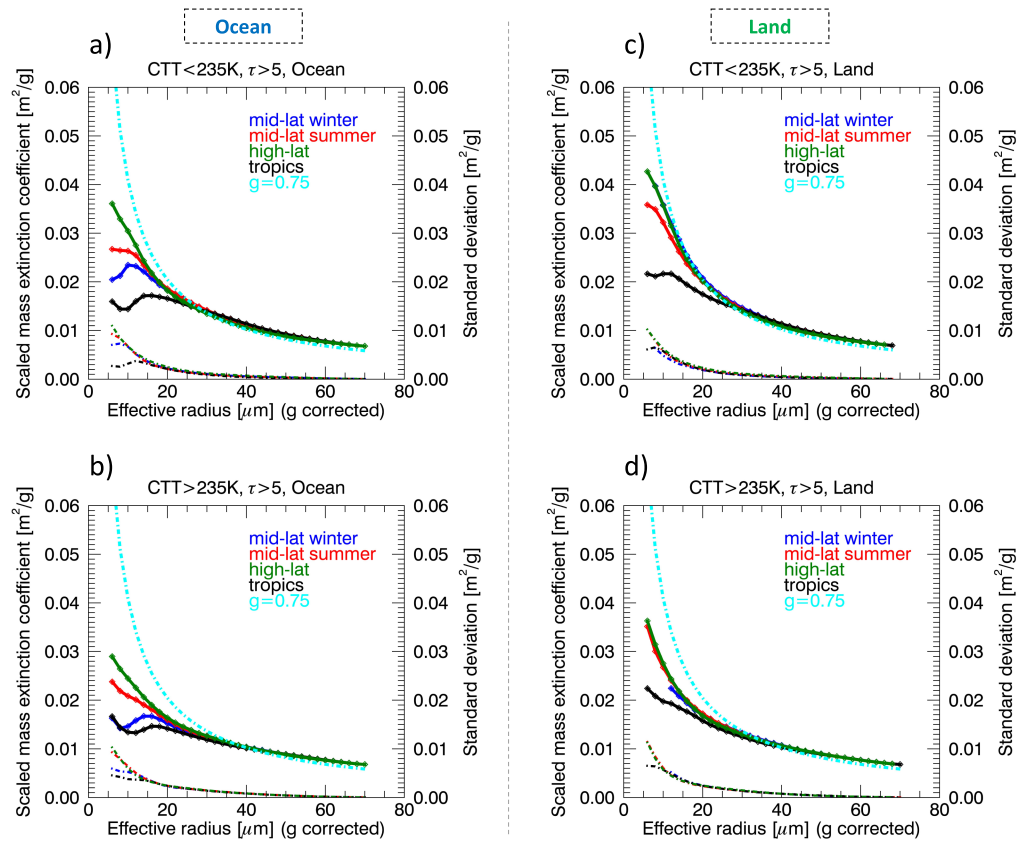


Figure 8. Statistics of scaled mass extinction coefficient as a function of cloud top temperature for clouds over ocean (a) and land (b). Line colors and types are the same as in previous figures.



**Figure 9.** Statistics of scaled mass extinction coefficient as a function of effective radius for cold (a, c) and warm (b, d) clouds over ocean (a, b) and land (c, d). Line colors and types are the same as in previous figures. The cyan dash-dotted lines represent the scaled mass extinction coefficient assuming a constant asymmetry parameter of 0.75.

(Figure 8b), with values that are generally about 20% larger indicating that, on average, ice clouds over land are more reflective than over ocean for a given liquid water path. Figure 9 shows  $\beta_s$  as a function of  $r_e$ , indicating that the decrease of  $g$  with increasing  $r_e$ , as shown in Figures 4 and 5, leads to a reduced variation of  $\beta_s$  with  $r_e$  compared to the case of constant  $g$ . This reduction implies that natural ice cloud reflectance is less sensitive to  $r_e$ , especially below 25  $\mu\text{m}$ , than predicted by commonly used optical models with  $g$  constant or increasing with  $r_e$  (e.g., Baum et al., 2011; Fu & Liou, 1993). To put the variation of  $\beta_s$  in perspective, we note that for a cloud layer with an ice water path of 100  $\text{g}/\text{m}^2$ , changing  $\beta_s$  from 0.010 to 0.015 leads to a relative increase in visible cloud reflectance of about 15–30%, depending on solar geometry.

We note that the scaled mass extinction coefficients are derived from the observations that pertain to cloud top and under the assumption of vertically invariant cloud layers. In reality, ice properties vary throughout the depth of a cloud layer. Generally, ice sizes increase with depth into a cloud layer relative to the top. Hence, the mass extinction coefficients estimate using cloud top effective radius may represent an upper limit. Furthermore, the asymmetry parameter may vary throughout the cloud depth affecting the scaled mass extinction coefficient. However, no reliable information is presently available on how asymmetry parameters may vary throughout a cloud column.

#### 4. Conclusions and Discussion

This paper presents ice microphysical properties at tops of optically thick ice clouds with cloud top temperatures below 273 K inferred from combined measurements of the POLDER and MODIS satellite instruments. Retrieved properties include the ice effective radius, aspect ratio of components of ice crystals, ice crystal distortion, and scattering asymmetry parameter. Our present analysis focuses on variations of average ice

crystal properties with cloud top temperature, latitude, season, and surface (land/ocean), as well as their covariation. Throughout this paper we show that the variation of ice crystal size and shape with temperature and the covariation of size and shape are consistent with ice crystal vapor growth theory and laboratory and in situ measurements. Retrieved effective radii are about 33  $\mu\text{m}$  on average over land and 38  $\mu\text{m}$  over ocean and are generally largest at cloud top temperatures between 240 and 250 K. Average asymmetry parameters over land and ocean are 0.75, which is consistent with the ice optical model used globally for the MODIS C6 cloud products. However, our data show considerably larger average asymmetry parameter values at temperatures higher than about 240 K, mainly because of decreased crystal distortion at those temperatures. Retrieved aspect ratios of components of crystals are close to 0.5 on average, but a distinct minimum down to mean values of 0.34 is apparent near 260 K. As a function of effective radius, average asymmetry parameters are found to generally decrease, while distortion parameters and aspect ratios increase. The effective radius and asymmetry parameter determine the reflection of a cloud layer with a given ice water path and the variations of effective radius and asymmetry parameter imply that optically thick ice clouds with cloud top temperatures near 250 K over ocean are the least reflective for a given ice water path. Furthermore, reflection of a cloud layer with a given ice water path generally increases as the effective radius decreases, but this increasing reflection is partly compensated by an increase of asymmetry parameter as implied from our data.

Our conclusion that covariations of ice crystal properties at tops of optically thick clouds with cloud top temperature and  $r_e$  are broadly consistent with theory, laboratory, and in situ data on ice growth rates, habit formation, and occurrence of crystal roughness or complexity, as demonstrated in this paper, may be viewed as somewhat surprising in its simplicity given the large number of other processes that govern ice crystal population properties and the expectation that  $r_e$  at cloud top will be an integral manifestation of processes at lower levels within updrafts, as far down as the liquid phase. This simplicity may be attributable to the temperature dependence of cloud top ice crystal size and shapes commonly being dominated by vapor growth at conditions consistent with cloud top, while size sorting, aggregation, riming, sublimation, and other processes likely lead to a wider range of properties deeper within the clouds than probed here. While processes such as increasing efficiency of size sorting with decreasing pressure may partly explain  $r_e$  decreasing with decreasing cloud top temperature, they fail to explain the transition to the opposite trend at higher temperatures, nor the occurrence of a distinct decrease in crystal aspect ratio near 260 K. We also note that there is no discontinuity in any of the observed ice properties near the homogenous freezing level, which may indicate little sensitivity to nucleation mode or that heterogeneous freezing processes dominate the observed cloud tops at all levels on average. These results provide valuable observational targets for studying ice formation and evolution processes using modeling studies.

Our results also suggest possible improvements of parameterizations for optical properties by including a representation of distortion level based on growth rate, as also supported by laboratory studies (Schnaiter et al., 2016; Voigtländer et al., 2018). The observed decrease in asymmetry parameter  $g$  with increasing size and decreasing temperature is in contrast with most optical models, which generally assume invariant  $g$  values or values *increasing* with size (e.g., Baum et al., 2011; Fu, 2007; Fu & Liou, 1993). Adopting an ice model consistent with our results for MODIS retrievals is expected to lead to an increased range in globally retrieved  $r_e$  and a reduction in  $r_e$  of about 25% for warm ice clouds in comparison to the C6 product (cf. Figures 2a and 3a to Figure S2). Moreover, the resulting reduction in variation of the scaled mass extinction parameters with  $r_e$  shown in Figure 9 indicates a reduced sensitivity of cloud reflection to  $r_e$  compared to earlier estimates (Fu & Liou, 1993). Radiative effects from changes in ice crystal size caused by changing concentrations of ice nuclei particles (Storelvmo, 2017; Zhao et al., 2018) may be overestimated by assuming optical models in which  $g$  increases with  $r_e$ . Our results and their consistency with laboratory and in situ data suggest that  $g$  and distortion level may be effectively parametrized as a function of  $r_e$  and temperature for use in cloud retrieval algorithms and other radiative transfer applications.

The analysis presented here is limited to statistics of ice-topped clouds with optical thickness larger than 5 and thus excludes optically thin cirrus. More detailed analyses of the retrieved ice microphysical properties as a function of, for example, cloud type, atmospheric state, collocated aerosol loading, size, and type merit further study. Since theory also correlates ice growth with supersaturation levels, future work may use water vapor data to relate the observed ice microphysical properties to humidity as well.

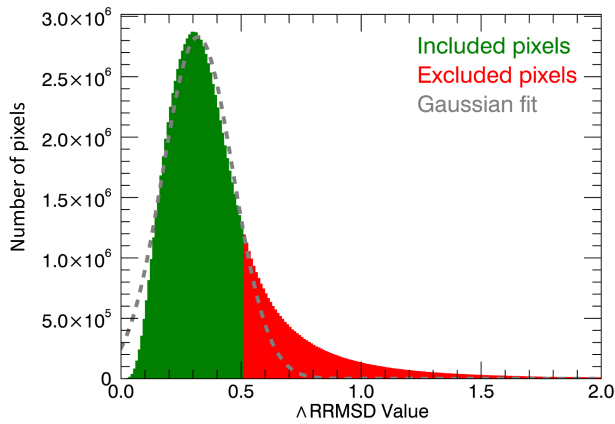


**Figure A1.** Histogram of minimum relative root-mean-squared difference ( $\Delta$ RRMSD) values for all selected POLDER ice cloud pixels. The gray line represents a Gaussian fit to the histogram. The green and red shaded parts of the data points are included and excluded, respectively, in our analysis.

Although we aimed to relate our results to previously published in situ and laboratory studies as best as possible, an analysis of ice properties observed in situ at cloud tops at a large range of temperatures would be valuable future work. However, current data sets may not be sufficient for such studies, as there remain large uncertainties, inconsistencies between probes, and gaps of information (Baumgardner et al., 2017; McFarquhar et al., 2017). For example, the depth within cloud relative to the cloud top at which the in situ measurements were collected is generally not available information. Furthermore, airborne campaigns are generally focused on obtaining statistics throughout the cloud column, meaning that the sampling at cloud tops at various temperatures is sparse. In addition, detailed observations on crystal shapes other than “habit” in addition to scattering properties are generally not available. Campaigns specifically targeting ice cloud tops at various temperatures and including new probes, such as the Particle Habit Imaging and Polar Scattering (PHIPS, Abdelmonem et al., 2011), may be advised.

## Appendix A: Relative Root-Mean-Squared Difference Calculation and Filtering

As explained in the main text, a relative root-mean-squared difference (RRMSD) is calculated between polarization measurements at the considered viewing angles for a given POLDER pixel and the corresponding

simulated values for each combination of particle aspect ratio and distortion level considered in the look-up table. For a pixel for which  $N$  polarized reflectance observations  $R_{p,meas}$  are available at scattering angles  $\Theta_n$ , this RRMSD associated with the combination of aspect ratio  $\alpha_i$  and distortion parameter  $\delta_j$  is given by

$$RRMSD(\alpha_i, \delta_j) = \sqrt{\frac{\sum_{n=1}^N \left[ 1 - \frac{R_{p,LUT}(\Theta_n, \alpha_i, \delta_j)}{R_{p,meas}(\Theta_n)} \right]^2}{N}}, \quad (A1)$$

where  $R_{p,LUT}$  is the simulated polarized reflectance for the particular scattering angle and combination of aspect ratio and distortion parameter.

The combination of aspect ratio and distortion value that leads to the minimum RRMSD (denoted as  $\Delta$ RRMSD) is considered the retrieved set for that pixel. However, effects caused by time differences between measurements at different viewing angles and different polarization angles, subpixel inhomogeneity, and possible other causes may lead to substantial variation of polarized reflectances with scattering angle that are not associated with ice crystals shape variations. These artifacts are expected to lead to a large value of the  $\Delta$ RRMSD. Hence, we aim to filter out retrievals affected by such artifacts by imposing an upper limit on the  $\Delta$ RRMSD. Since the artifacts affecting the polarized reflectances are difficult to characterize using simulated measurements, we aim to define the upper limit of  $\Delta$ RRMSD empirically. Figure A1 shows a histogram of all  $\Delta$ RRMSD values inferred for the data set described in the main text. The shape of the histogram resembles a skewed Gaussian with a long positive tail. A Gaussian function is fitted to the distribution (gray dashed line), which has a mean value of 0.32 and standard deviation of 0.15. Considering the mean values plus one standard deviation is at approximately 0.5, we have chosen to include only data with  $\Delta$ RRMSD values below 0.5 in our analysis. Note that selecting a larger limit (e.g., 0.8) does not qualitatively change any of the conclusions reached in this study.

## References

- Abdelmonem, A., Schnaiter, M., Amsler, P., Hesse, E., Meyer, J., & Leisner, T. (2011). First correlated measurements of the shape and light scattering properties of cloud particles using the new Particle Habit Imaging and Polar Scattering (PHIPS) probe. *Atmospheric Measurement Techniques*, 4(10), 2125–2142. <https://doi.org/10.5194/amt-4-2125-2011>. (online) Available from: <http://www.atmos-meas-tech.net/4/2125/2011/amt-4-2125-2011.html>

## Acknowledgments

The authors declare no competing interests. The ice crystal shape and asymmetry data set generated during the current study are available in the Open Science Framework repository (<https://osf.io/c7g58/>). The POLDER-MODIS combined data set analyzed during the current study is available from the ICARE Data and Services Center (<http://www.icare.univ-lille1.fr/>). We would like to thank Professor Jerry Harrington at Penn State University for providing the inherent growth ratio data. We thank Professor Ralf Bennartz at Vanderbilt University for his suggestions to compare size profiles with ice crystal relative growth rates. We thank three anonymous reviewers for their helpful comments. Funding for this work is provided by NASA through Grant NNX14AJ28G.

- Bacon, N. J., Baker, M. B., & Swanson, B. D. (2003). Initial stages in the morphological evolution of vapour-grown ice crystals: A laboratory investigation. *Quarterly Journal of the Royal Meteorological Society*, *129*(591), 1903–1927. <https://doi.org/10.1256/qj.02.04>
- Bailey, M. P., & Hallett, J. (2004). Growth rates and habits of ice crystals between  $-20^{\circ}$  and  $-70^{\circ}\text{C}$ . *Journal of the Atmospheric Sciences*, *61*(5), 514–544. [https://doi.org/10.1175/1520-0469\(2004\)061<0514:GRAHOI>2.0.CO;2](https://doi.org/10.1175/1520-0469(2004)061<0514:GRAHOI>2.0.CO;2)
- Bailey, M. P., & Hallett, J. (2009). A comprehensive habit diagram for atmospheric ice crystals: Confirmation from the laboratory, AIRS II, and other field studies. *Journal of the Atmospheric Sciences*, *66*(9), 2888–2899. <https://doi.org/10.1175/2009JAS2883.1>
- Barkstrom, B. R. (1978). Some effects of 8–12  $\mu\text{m}$  radiant energy transfer on the mass and heat budgets of cloud droplets. *Journal of the Atmospheric Sciences*, *35*(4), 665–673. [https://doi.org/10.1175/1520-0469\(1978\)035<0665:SEORET>2.0.CO;2](https://doi.org/10.1175/1520-0469(1978)035<0665:SEORET>2.0.CO;2)
- Baum, B. A., Yang, P., Heymsfield, A. J., Schmitt, C. G., Xie, Y., Bansemmer, A., et al. (2011). Improvements in shortwave bulk scattering and absorption models for the remote sensing of ice clouds. *Journal of Applied Meteorology and Climatology*, *50*(5), 1037–1056. <https://doi.org/10.1175/2010JAMC2608.1>
- Baumgardner, D., et al. (2017). Cloud ice properties: In situ measurement challenges. *Meteorological monographs*, *58*, 9.1–9.23. <https://doi.org/10.1175/AMSMONOGRAPHS-D-16-0011.1>
- Bi, L., Yang, P., Liu, C., Yi, B., Baum, B. A., van Diedenhoven, B., & Iwabuchi, H. (2014). Assessment of the accuracy of the conventional ray-tracing technique: Implications in remote sensing and radiative transfer involving ice clouds. *Journal of Quantitative Spectroscopy & Radiative Transfer*, *146*, 158–174. <https://doi.org/10.1016/j.jqsrt.2014.03.017>
- Bohren, C. F., & Albrecht, B. A. (1998). *Atmospheric thermodynamics*. New York: Oxford University Press.
- Boucher, O., Randall, D., Artaxo, P., Bretherton, C., Feingold, G., Forster, P., et al. (2013). Clouds and aerosols. In T. F. Stocker et al. (Eds.), *Climate Change 2013: The Physical Science Basis. Contribution of Working Group I to the Fifth Assessment Report of the Intergovernmental Panel on Climate Change* (Chap. 7, pp. 571–657). Cambridge, UK: Cambridge University Press. <https://doi.org/10.1017/CBO9781107415324.016>
- Bréon, F.-M., & Dubrulle, B. (2004). Horizontally oriented plates in clouds. *Journal of the Atmospheric Sciences*, *61*(23), 2888–2898. <https://doi.org/10.1175/JAS-3309.1>
- Butterfield, N., Rowe, P. M., Stewart, E., Roesel, D., & Neshyba, S. (2017). Quantitative three-dimensional ice roughness from scanning electron microscopy. *Journal of Geophysical Research*, *122*(5), 3023–3041. <https://doi.org/10.1002/2016JD026094>
- Chen, J. P., & Lamb, D. (1994). The theoretical basis for the parameterization of ice crystal habits: Growth by vapor deposition. *Journal of the Atmospheric Sciences*, *51*(9), 1206–1222. [https://doi.org/10.1175/1520-0469\(1994\)051<1206:TTBFTP>2.0.CO;2](https://doi.org/10.1175/1520-0469(1994)051<1206:TTBFTP>2.0.CO;2)
- Cox, C., & Munk, W. (1956). Slopes of the sea surface deduced from photographs of sun glitter. *Bulletin of the Scripps Institution of Oceanography*, *6*(9), 401–488.
- Ding, J., Yang, P., Kattawar, G. W., King, M. D., Platnick, S., & Meyer, K. G. (2017). Validation of quasi-invariant ice cloud radiative quantities with MODIS satellite-based cloud property retrievals. *Journal of Quantitative Spectroscopy and Radiation Transfer*, *194*, 47–57. <https://doi.org/10.1016/j.jqsrt.2017.03.025>
- Fauchez, T., Platnick, S., Sourdeval, O., Wang, C., Meyer, K., Cornet, C., & Szczap, F. (2018). Cirrus horizontal heterogeneity and 3D radiative effects on cloud optical property retrievals from MODIS near to thermal infrared channels as a function of spatial resolution. *Journal of Geophysical Research*. <https://doi.org/10.1029/2018JD028726>
- Foot, J. S. (1988). Some observations of the optical properties of clouds. II: Cirrus. *Journal of the Royal Meteorological Society*, *114*(479), 145–164. <https://doi.org/10.1002/qj.49711447908>
- Fridlind, A. M., Atlas, R., van Diedenhoven, B., Um, J., McFarquhar, G. M., Ackerman, A. S., et al. (2016). Derivation of physical and optical properties of mid-latitude cirrus ice crystals for a size-resolved cloud microphysics model. *Atmospheric Chemistry and Physics*, *16*(11), 7251–7283. <https://doi.org/10.5194/acp-16-7251-2016>
- Fu, Q. (2007). A new parameterization of an asymmetry factor of cirrus clouds for climate models. *Journal of the Atmospheric Sciences*, *64*(11), 4140. <https://doi.org/10.1175/2007JAS2289.1>
- Fu, Q., & Liou, K. N. (1993). Parameterization of the radiative properties of cirrus clouds. *Journal of the Atmospheric Sciences*, *50*(13), 2008–2025. [https://doi.org/10.1175/1520-0469\(1993\)050<2008:POTRPO>2.0.CO;2](https://doi.org/10.1175/1520-0469(1993)050<2008:POTRPO>2.0.CO;2)
- Fukuta, N., & Takahashi, T. (1999). The growth of atmospheric ice crystals: A summary of findings in vertical supercooled cloud tunnel studies. *Journal of the Atmospheric Sciences*, *56*(12), 1963–1979. [https://doi.org/10.1175/1520-0469\(1999\)056<1963:TGOAIC>2.0.CO;2](https://doi.org/10.1175/1520-0469(1999)056<1963:TGOAIC>2.0.CO;2)
- Geogdzhayev, I., & van Diedenhoven, B. (2016). The effect of roughness model on scattering properties of ice crystals. *Journal of Quantitative Spectroscopy & Radiative Transfer*, *178*. <https://doi.org/10.1016/j.jqsrt.2016.03.001>
- de Haan, J., Bosma, P., & Hovenier, J. (1987). The adding method for multiple scattering calculations of polarized light. *Astronomy and Astrophysics*, *183*(2), 371–391.
- Hashino, T., & Tripoli, G. J. (2007). The spectral ice habit prediction system (SHIPS). Part I: Model description and simulation of the vapor deposition process. *Journal of the Atmospheric Sciences*, *64*(7), 2210–2237. <https://doi.org/10.1175/JAS3963.1>
- Hashino, T., & Tripoli, G. J. (2011). The spectral ice habit prediction system (SHIPS). Part III: Description of the ice particle model and the habit-dependent aggregation model. *Journal of the Atmospheric Sciences*, *68*(6), 1125–1141. <https://doi.org/10.1175/2011JAS3666.1>
- Heymsfield, A. J., Miloshevich, L. M., Heymsfield, A. J., & Miloshevich, L. M. (2003). Parameterizations for the cross-sectional area and extinction of cirrus and stratiform ice cloud particles. *Journal of the Atmospheric Sciences*, *60*(7), 936–956. [https://doi.org/10.1175/1520-0469\(2003\)060<0936:PFTCSA>2.0.CO;2](https://doi.org/10.1175/1520-0469(2003)060<0936:PFTCSA>2.0.CO;2)
- Hioki, S., Yang, P., Baum, B. A., Platnick, S., Meyer, K. G., King, M. D., & Riedi, J. (2016). Degree of ice particle surface roughness inferred from polarimetric observations. *Atmospheric Chemistry and Physics*, *16*(12), 7545–7558. <https://doi.org/10.5194/acp-16-7545-2016>
- Holz, R. E., et al. (2016). Resolving ice cloud optical thickness biases between CALIOP and MODIS using infrared retrievals. *Atmospheric Chemistry and Physics*, *16*(8), 5075–5090. <https://doi.org/10.5194/acp-16-5075-2016>
- Hong, G., & Minnis, P. (2015). Effects of spherical inclusions on scattering properties of small ice cloud particles. *Journal of Geophysical Research*, *120*(7), 2951–2969. <https://doi.org/10.1002/2014JD022494>
- Iaquinta, J., Isaka, H., & Personne, P. (1995). Scattering phase function of bullet rosette ice crystals. *Journal of the Atmospheric Sciences*, *52*(9), 1401–1413. [https://doi.org/10.1175/1520-0469\(1995\)052<1401:SPFOBR>2.0.CO;2](https://doi.org/10.1175/1520-0469(1995)052<1401:SPFOBR>2.0.CO;2)
- Järvinen, E., et al. (2018). Additional global climate cooling by clouds due to ice crystal complexity. *Atmospheric Chemistry and Physics*, *18*, 15,767–15,781. <https://doi.org/10.5194/acp-2018-491>
- Jensen, A. A., Harrington, J. Y., Morrison, H., & Milbrandt, J. A. (2017). Predicting ice shape evolution in a bulk microphysics model. *Journal of the Atmospheric Sciences*, *74*(6), 2081–2104. <https://doi.org/10.1175/JAS-D-16-0350.1>
- Kahn, B. H., Takahashi, H., Stephens, G. L., Yue, Q., Delanoë, J., Manipon, G., et al. (2018). Ice cloud microphysical trends observed by the atmospheric infrared sounder. *Atmospheric Chemistry and Physics*, *18*(14), 10,715–10,739. <https://doi.org/10.5194/acp-18-10715-2018>

- Korolev, A., & Isaac, G. A. (2006). Relative humidity in liquid, mixed-phase, and ice clouds. *Journal of the Atmospheric Sciences*, 63(11), 2865–2880. <https://doi.org/10.1175/JAS3784.1>
- Lawson, R. P., et al. (2019). A review of ice particle shapes in cirrus formed in situ and in anvils. *Journal of Geophysical Research*, 2018JD030122. <https://doi.org/10.1029/2018JD030122>
- Liu, C., Panetta, R. L., & Yang, P. (2014). The effective equivalence of geometric irregularity and surface roughness in determining particle single-scattering properties. *Optics Express*, 22(19), 23,620–23,627. <https://doi.org/10.1364/OE.22.023620>
- Luo, Z., Liu, G. Y., Stephens, G. L., & Johnson, R. H. (2009). Terminal versus transient cumulus congestus: A CloudSat perspective. *Geophysical Research Letters*, 36(5), L05808. <https://doi.org/10.1029/2008GL036927>
- Macke, A., Mueller, J., & Raschke, E. (1996). Single scattering properties of atmospheric ice crystals. *Journal of the Atmospheric Sciences*, 53(19), 2813–2825.
- Magee, N. B., Miller, A., Amaral, M., & Cumiskey, A. (2014). Mesoscopic surface roughness of ice crystals pervasive across a wide range of ice crystal conditions. *Atmospheric Chemistry and Physics*, 14(22), 12,357–12,371. <https://doi.org/10.5194/acp-14-12357-2014>
- McFarquhar, G. M., Baumgardner, D., Bansemir, A., Abel, S. J., Crosier, J., French, J., et al. (2017). Processing of ice cloud in situ data collected by bulk water, scattering, and imaging probes: Fundamentals, uncertainties, and efforts toward consistency. *Meteorological Monographs*, 58, 11.1–11.33. <https://doi.org/10.1175/AMSMONOGRAPHIS-D-16-0007.1>. (online) Available from: <http://journals.ametsoc.org/doi/10.1175/AMSMONOGRAPHIS-D-16-0007.1>
- Mitchell, D. L. (1996). Use of mass- and area-dimensional power laws for determining precipitation particle terminal velocities. *Journal of the Atmospheric Sciences*, 53(12), 1710–1723.
- Neshyba, S. P., Lowen, B., Benning, M., Lawson, A., & Rowe, P. M. (2013). Roughness metrics of prismatic facets of ice. *Journal of Geophysical Research*, 118(8), 3309–3318. <https://doi.org/10.1002/jgrd.50357>
- Pfalzgraff, W. C., Hulscher, R. M., & Neshyba, S. P. (2010). Scanning electron microscopy and molecular dynamics of surfaces of growing and ablating hexagonal ice crystals. *Atmospheric Chemistry and Physics*, 10(6), 2927–2935. <https://doi.org/10.5194/acp-10-2927-2010>
- Platnick, S., Meyer, K. G., King, M. D., Wind, G., Amarasinghe, N., Marchant, B., et al. (2017). The MODIS cloud optical and microphysical products: Collection 6 updates and examples from Terra and Aqua. *IEEE Transactions on Geoscience and Remote Sensing*, 55(1), 502–525. <https://doi.org/10.1109/TGRS.2016.2610522>
- Platt, C. M. R. (1997). A parameterization of the visible extinction coefficient of ice clouds in terms of the ice/water content. *Journal of the Atmospheric Sciences*, 54(16), 2083–2098. [https://doi.org/10.1175/1520-0469\(1997\)054<2083:APOTVE>2.0.CO;2](https://doi.org/10.1175/1520-0469(1997)054<2083:APOTVE>2.0.CO;2)
- Pruppacher, H. R., & Klett, J. D. (1997). *Microphysics of clouds and precipitation*, (2nd ed.). Dordrecht, Netherlands: Kluwer Academic Publishers.
- Riedi, J., Marchant, B., Platnick, S., Baum, B. A., Thieuleux, F., Oudard, C., et al. (2010). Cloud thermodynamic phase inferred from merged POLDER and MODIS data. *Atmospheric Chemistry and Physics*, 10(23), 11,851–11,865. <https://doi.org/10.5194/acp-10-11851-2010>
- Rossow, W. B., & Schiffer, R. A. (1999). Advances in understanding clouds from ISCCP. *Bulletin of the American Meteorological Society*, 80(11), 2261–2287. [https://doi.org/10.1175/1520-0477\(1999\)080<2261:AIUCFI>2.0.CO;2](https://doi.org/10.1175/1520-0477(1999)080<2261:AIUCFI>2.0.CO;2)
- Schmitt, C. G., Heymsfield, A. J., Connolly, P., Järvinen, E., & Schnaiter, M. (2016). A global view of atmospheric ice particle complexity. *Geophysical Research Letters*, 43(22), 11,913–11,920. <https://doi.org/10.1002/2016GL071267>
- Schmitt, C. G., Heymsfield, A. J., Schmitt, C. G., & Heymsfield, A. J. (2010). The dimensional characteristics of ice crystal aggregates from fractal geometry. *Journal of the Atmospheric Sciences*, 67(5), 1605–1616. <https://doi.org/10.1175/2009JAS3187.1>
- Schnaiter, M., Järvinen, E., Vochezer, P., Abdelmonem, A., Wagner, R., Jourdan, O., et al. (2016). Cloud chamber experiments on the origin of ice crystal complexity in cirrus clouds. *Atmospheric Chemistry and Physics*, 16(8), 5091–5110. <https://doi.org/10.5194/acp-16-5091-2016>
- Stephens, G. L., Gabriel, P. M., & Partain, P. T. (2001). Parameterization of atmospheric radiative transfer. Part I: Validity of simple models. *Journal of the Atmospheric Sciences*, 58(22), 3391–3409. [https://doi.org/10.1175/1520-0469\(2001\)058<3391:POARTP>2.0.CO;2](https://doi.org/10.1175/1520-0469(2001)058<3391:POARTP>2.0.CO;2)
- Storelvmo, T. (2017). Aerosol effects on climate via mixed-phase and ice clouds. *Annual Review of Earth and Planetary Sciences*, 45(1), 199–222. <https://doi.org/10.1146/annurev-earth-060115-012240>
- Twomey, S., & Bohren, C. F. (1980). Simple approximations for calculations of absorption in clouds. *Journal of the Atmospheric Sciences*, 37(9), 2086–2095. [https://doi.org/10.1175/1520-0469\(1980\)037<2086:SAFCOA>2.0.CO;2](https://doi.org/10.1175/1520-0469(1980)037<2086:SAFCOA>2.0.CO;2)
- Um, J., & McFarquhar, G. M. (2007). Single-scattering properties of aggregates of bullet rosettes in cirrus. *Journal of Applied Meteorology and Climatology*, 46, 757–775. <https://doi.org/10.1175/JAM2501.1>
- Um, J., & McFarquhar, G. M. (2009). Single-scattering properties of aggregates of plates. *Quarterly Journal of the Royal Meteorological Society*, 135(639), 291–304. <https://doi.org/10.1002/qj.378>
- Um, J., & McFarquhar, G. M. (2015). Formation of atmospheric halos and applicability of geometric optics for calculating single-scattering properties of hexagonal ice crystals: Impacts of aspect ratio and ice crystal size. *Journal of Quantitative Spectroscopy & Radiative Transfer*, 165, 134–152. <https://doi.org/10.1016/J.JQSRT.2015.07.001>
- van Diedenhoven, B. (2014). The prevalence of the 22° halo in cirrus clouds. *Journal of Quantitative Spectroscopy and Radiative Transfer*, 146. <https://doi.org/10.1016/j.jqsrt.2014.01.012>
- van Diedenhoven, B. (2018). Remote sensing of crystal shapes in ice clouds. In *Springer Series in Light Scattering*, (pp. 197–250). Cham: Springer.
- van Diedenhoven, B., Ackerman, A. S., Cairns, B., & Fridlind, A. M. (2014). A flexible parameterization for shortwave optical properties of ice crystals. *Journal of the Atmospheric Sciences*, 71(5), 1763–1782. <https://doi.org/10.1175/JAS-D-13-0205.1>
- van Diedenhoven, B., Ackerman, A. S., Fridlind, A. M., & Cairns, B. (2016). On averaging aspect ratios and distortion parameters over ice crystal population ensembles for estimating effective scattering asymmetry parameters. *Journal of the Atmospheric Sciences*, 73(2), 775–787. <https://doi.org/10.1175/JAS-D-15-0150.1>
- van Diedenhoven, B., Cairns, B., Fridlind, A. M., Ackerman, A. S., & Garrett, T. J. (2013). Remote sensing of ice crystal asymmetry parameter using multi-directional polarization measurements—Part 2: Application to the Research Scanning Polarimeter. *Atmospheric Chemistry and Physics*, 13(6), 3185–3203. <https://doi.org/10.5194/acp-13-3185-2013>
- van Diedenhoven, B., Cairns, B., Geogdzhayev, I. V., Fridlind, A. M., Ackerman, A. S., Yang, P., & Baum, B. A. (2012). Remote sensing of ice crystal asymmetry parameter using multi-directional polarization measurements—Part 1: Methodology and evaluation with simulated measurements. *Atmospheric Measurement Techniques*, 5(10), 2361–2374. <https://doi.org/10.5194/amt-5-2361-2012>
- van Diedenhoven, B., Fridlind, A. M., Ackerman, A. S., & Cairns, B. (2012). Evaluation of hydrometeor phase and ice properties in cloud-resolving model simulations of tropical deep convection using radiance and polarization measurements. *Journal of the Atmospheric Sciences*, 69(11), 3290–3314. <https://doi.org/10.1175/JAS-D-11-0314.1>
- van Diedenhoven, B., Fridlind, A. M., Cairns, B., & Ackerman, A. S. (2014). Variation of ice crystal size, shape, and asymmetry parameter in tops of tropical deep convective clouds. *Journal of Geophysical Research*, 119(20), 11,809–11,825. <https://doi.org/10.1002/2014JD022385>

- van Diedenhoven, B., Fridlind, A. M., Cairns, B., Ackerman, A. S., & Yorks, J. E. (2016). Vertical variation of ice particle size in convective cloud tops. *Geophysical Research Letters*, *43*(9), 4586–4593. <https://doi.org/10.1002/2016GL068548>
- Vogelmann, A. M., & Ackerman, T. P. (1995). Relating cirrus cloud properties to observed fluxes: A critical assessment. *Journal of the Atmospheric Sciences*, *52*(23), 4285–4301. [https://doi.org/10.1175/1520-0469\(1995\)052<4285:RCCPTO>2.0.CO;2](https://doi.org/10.1175/1520-0469(1995)052<4285:RCCPTO>2.0.CO;2)
- Voigtländer, J., Chou, C., Bieligk, H., Clauss, T., Hartmann, S., Herenz, P., et al. (2018). Surface roughness during depositional growth and sublimation of ice crystals. *Atmospheric Chemistry and Physics*, *18*(18), 13,687–13,702. <https://doi.org/10.5194/acp-18-13687-2018>
- Waliser, D. E., et al. (2009). Cloud ice: A climate model challenge with signs and expectations of progress. *J. Geophys. Res.*, *114*(3), D00A21. <https://doi.org/10.1029/2008JD010015>
- Yang, P., Hong, G., Kattawar, G. W., Minnis, P., & Hu, Y. (2008). Uncertainties associated with the surface texture of ice particles in satellite-based retrieval of cirrus clouds: Part II—Effect of particle surface roughness on retrieved cloud optical thickness and effective particle size. *IEEE Transactions on Geoscience and Remote Sensing*, *46*(7), 1948–1957. <https://doi.org/10.1109/TGRS.2008.916472>
- Yang, P., Kattawar, G. W., Hong, G., Minnis, P., & Hu, Y. X. (2008). Uncertainties associated with the surface texture of ice particles in satellite-based retrieval of cirrus clouds—Part I: Single-scattering properties of ice crystals with surface roughness. *IEEE Transactions on Geoscience and Remote Sensing*, *46*(7), 1940–1947. <https://doi.org/10.1109/TGRS.2008.916471>
- Yang, P., Liou, K.-N., Bi, L., Liu, C., Yi, B., & Baum, B. A. (2015). On the radiative properties of ice clouds: Light scattering, remote sensing, and radiation parameterization. *Advances in Atmospheric Sciences*, *32*(1), 32–63. <https://doi.org/10.1007/s00376-014-0011-z>
- Yuan, T., & Li, Z. (2010). General macro- and microphysical properties of deep convective clouds as observed by MODIS. *Journal of Climate*, *23*(13), 3457–3473. <https://doi.org/10.1175/2009JCLI3136.1>
- Yuan, T., Martins, J. V., Li, Z., & Remer, L. A. (2010). Estimating glaciation temperature of deep convective clouds with remote sensing data. *Geophysical Research Letters*, *37*(8), 1–5. <https://doi.org/10.1029/2010GL042753>
- Zhang, Z., Werner, F., Cho, H.-M., Wind, G., Platnick, S., Ackerman, A. S., et al. (2016). A framework based on 2-D Taylor expansion for quantifying the impacts of subpixel reflectance variance and covariance on cloud optical thickness and effective radius retrievals based on the bispectral method. *Journal of Geophysical Research*, *121*(12), 7007–7025. <https://doi.org/10.1002/2016JD024837>
- Zhao, B., Liou, K. N., Gu, Y., Jiang, J. H., Li, Q., Fu, R., et al. (2018). Impact of aerosols on ice crystal size. *Atmospheric Chemistry and Physics*, *18*(2), 1065–1078. <https://doi.org/10.5194/acp-18-1065-2018>
- Zhou, C., Yang, P., Dessler, A. E., Hu, Y., & Baum, B. A. (2012). Study of horizontally oriented ice crystals with CALIPSO observations and comparison with Monte Carlo radiative transfer simulations. *Journal of Applied Meteorology and Climatology*, *59*(7), 1426–1439. <https://doi.org/10.1175/JAMC-D-11-0265.1>